

Testing Chern-Simons Modified Gravity with Gravitational-Wave Detections of Extreme-Mass-Ratio Binaries

Priscilla Canizares,^{1,2,*} Jonathan R. Gair,^{1,†} and Carlos F. Sopuerta^{2,‡}

¹*Institute of Astronomy, Madingley Road, Cambridge, CB30HA, United Kingdom*

²*Institut de Ciències de l'Espai (CSIC-IEEC), Campus UAB, Torre C5 parells, 08193 Bellaterra, Spain*

(Dated: March 3, 2013)

The detection of gravitational waves from extreme-mass-ratio inspirals (EMRIs), comprising a stellar-mass compact object orbiting around a massive black hole, is one of the main targets for low-frequency gravitational-wave detectors in space, like the Laser Interferometer Space Antenna (LISA) or evolved LISA/New Gravitational Observatory (eLISA/NGO). The long-duration gravitational-waveforms emitted by such systems encode the structure of the strong field region of the massive black hole, in which the inspiral occurs. The detection and analysis of EMRIs will therefore allow us to study the geometry of massive black holes and determine whether their nature is as predicted by General Relativity and even to test whether General Relativity is the correct theory to describe the dynamics of these systems. To achieve this, EMRI modeling in alternative theories of gravity is required to describe the generation of gravitational waves. However, up to now, only a restricted class of theories has been investigated. In this paper, we explore to what extent EMRI observations with a space-based gravitational-wave observatory like LISA or eLISA/NGO might be able to distinguish between General Relativity and a particular modification of it, known as Dynamical Chern-Simons Modified Gravity. Our analysis is based on a parameter estimation study that uses approximate gravitational waveforms obtained via a radiative-adiabatic method. In this framework, the trajectory of the stellar object is modeled as a sequence of geodesics in the spacetime of the modified-gravity massive black hole. The evolution between geodesics is determined by flux formulae based on general relativistic post-Newtonian and black hole perturbation theory computations. Once the trajectory of the stellar compact object has been obtained, the waveforms are computed using the standard multipole formulae for gravitational radiation applied to this trajectory. Our analysis is restricted to a five-dimensional subspace of the EMRI configuration space, including a Chern-Simons parameter that controls the strength of gravitational deviations from General Relativity. We find that, if Dynamical Chern-Simons Modified Gravity is the correct theory, an observatory like LISA or even eLISA/NGO should be able to measure the Chern-Simons parameter with fractional errors below 5%. If General Relativity is the true theory, these observatories should put bounds on this parameter at the level $\xi^{1/4} < 10^4$ km, which is four orders of magnitude better than current Solar System bounds.

PACS numbers: 04.30.Db, 04.30.-w, 04.50.Kd, 95.30.Sf, 97.10.Sj

I. INTRODUCTION

There is strong observational evidence for the existence of black holes in galactic x-ray binary systems, seen as ultraluminous x-ray sources, and in the centers of galaxies, seen as active galactic nuclei (see, e.g. [1]). Indeed, observations carried out by space- and ground-based telescopes suggest the presence of a dark compact object, likely a massive black hole (MBH), at the center of most observed galaxies (see [2] and references therein). In a typical galaxy, the MBH is surrounded by around $10^7 - 10^8$ stars forming a cusp or core (see, e.g. [3]). As a consequence of relaxation, mass segregation and large scattering encounters between the stars, stellar compact objects (SCOs) may be perturbed onto orbits that pass sufficiently close to the MBH and become gravitationally bound forming a binary system. Therefore, the capture

of a SCO by a MBH is likely to be a frequent phenomenon in the Universe.

Once the SCO has become bound to the MBH, it starts a slow inspiral driven by the emission of gravitational waves (GWs). During this process, the system loses energy and angular momentum and the orbit of the SCO circularizes and shrinks adiabatically, i.e. on a timescale much longer than the orbital period. The loss of energy and angular momentum occurs initially in bursts, when the object passes through the orbital pericenter, but eventually the gravitational radiation is being emitted continuously until the object reaches the innermost stable orbit and plunges into the MBH. For EMRIs whose GW frequencies lie in the sensitivity band of space-based GW detectors, like LISA (Laser Interferometer Space Antenna [4, 5]) or eLISA/NGO (evolved LISA/New Gravitational Observatory [6, 7]), the central MBH must have mass in the range, $M_{\bullet} \sim 10^4 - 10^7 M_{\odot}$. The systems of interest must also have a SCO compact enough to avoid tidal-disruption and so the SCO must be a stellar mass black hole ($m_{\star} \approx 1 - 50 M_{\odot}$), a neutron star ($m_{\star} \approx 1.4 M_{\odot}$) or a white dwarf ($m_{\star} \approx 0.6 M_{\odot}$). The

* pcm@ast.cam.ac.uk

† jrg23@cam.ac.uk

‡ sopuerta@ieec.uab.es

typical mass ratios, $\mu = m_*/M_\bullet$, of EMRI systems are therefore in the range $\sim 10^{-6} - 10^{-4}$.

The strongest detectable EMRI signals are unlikely to be any closer than a luminosity distance $D \sim 1$ Gpc [8], at which distance the instantaneous amplitude of the measured EMRI signal is an order of magnitude below the level of instrumental noise and the GW foreground from galactic white-dwarf binaries. EMRI detection will therefore rely on matched filtering of the detected data stream with a bank of templates of the possible signals that might be present in the data. During the last year before plunge, an EMRI will generate $\sim 1/\mu$ gravitational waveform cycles in the LISA band [9]. During this time, the orbit of the SCO tracks the strong field geometry in the vicinity of the MBH and maps out the (multipolar) structure of the MBH spacetime [10] in the emitted GWs.

GWs from EMRIs are generated in the strong field region close to the MBH and therefore probe General Relativity (GR) in a regime which, up to now, has not been reached observationally. If GR is the true theory of gravity describing EMRI dynamics, their waveforms will determine the parameters of the system with very high precision. However, if the central MBH is not described by the Kerr metric or GR does not properly describe the binary dynamics in the strong field regime, and we assume GR when constructing our detection templates, we will obtain incorrect results from GW observations. Therefore, there is a strong motivation for studying what kind of modifications to the dynamics of EMRIs one could expect from considering well-motivated theories of gravity other than GR. To that end, we must understand how the signals are modified in these alternative theories so that we are able to detect and quantify deviations from GR.

The use of EMRI observations for such tests of fundamental physics has been explored by several authors (see [11] and references therein), but the majority of that work has focussed on using the observations to constrain the properties of “bumpy” black holes. These are solutions to the field equations of general relativity that represent spacetimes that differ from the Kerr solution by an amount controlled by a tunable deviation parameter. EMRI observations will be able to place bounds on the size of deviations of the forms considered [12–16]. However, this is not necessarily a test of general relativity, since the bumpy black holes are constructed within that theory. It is rather a test of the “no-hair” property of black holes (stationary astrophysical black holes are described by the 2-parameter (mass and spin) family of spacetime geometries of Kerr [17]) and hence the auxiliary assumptions that go into the no-hair conjecture. Hence, “bumpy” black holes are actually a test of the Kerr geometry assuming GR is the correct theory of gravity.

Due to the myriad of alternative theories of gravity available, the questions that arise are: Which kind of theory do we choose to compare against? What new fea-

tures might we expect to observe in the GW signals that might allow us to distinguish this theory from GR? In this paper we address these different questions and explore the capability of a space-based detector like LISA to discriminate between GR and an alternative theory of gravity. In particular, we focus in a modification of GR constructed by the addition of a Chern-Simons (CS) gravitational term (also known as the Pontryagin invariant) to the action. Interest in this theory was initiated with the work of Jackiw and Pi [18] where gravitational parity violation was investigated. Such a term appears in four-dimensional compactifications of perturbative string theory due to the Green-Schwarz anomaly-canceling mechanism [19] and also in loop quantum gravity when the Barbero-Immirzi parameter is promoted to a scalar field coupled to the Nieh-Yan invariant [20–22]. Moreover, the Pontryagin term is unavoidable in an effective field theory (see [23] in the context of cosmological inflation). In the approach of Jackiw and Pi, the Pontryagin term is introduced in the action multiplied by a scalar function and, in this way, it contributes to the field equations (in a four-dimensional spacetime the Pontryagin term is a topological invariant and hence does not contribute to the field equations), but this field is not dynamical. That is, it is a given function of the spacetime coordinates. This version of CS modified gravity has been extensively studied and it has been shown to be dynamically too restrictive and, for instance, generic oscillations of non-rotating Schwarzschild black hole are not allowed [24]. In addition there are problems with the uniqueness of solutions of the theory [25]. For these reasons we focus on the version of the theory in which the CS scalar field is dynamical, i.e. Dynamical Chern-Simons Modified Gravity (DCSMG), see [26] for a review of CS modified gravity.

The first study of EMRIs in DCSMG was done in [27], where the main ingredients of the problem were discussed and a simple waveform model was put forward. This model used the so-called *semi-relativistic* approximation, in which the trajectories are geodesics and the waveforms are built by using a standard multipolar expansion of the gravitational radiation. Then, differences between the GR and DCSMG waveforms were studied and also some predictions for the relative dephasing of the waves were made. However, this work relied on the assumption that radiation reaction (RR) effects, i.e. the effects that arise from the interaction of the SCO with its own gravitational field would allow one to distinguish between GR and DCSMG. Without RR the harmonic structure of the waveforms is going to be very similar and hence it is likely that it would be always possible to match a signal with both GR and DCSMG template waveform models. On the other hand, in a recent study [28], corrections to the gravitational- and scalar-wave fluxes for circular orbits around a non-rotating MBH in CS gravity have been computed using perturbation theory. This type of computations are very promising and can complement the work we present in this paper.

In this paper we go beyond the model of [27] by including two important additional ingredients: (i) RR effects based on a hybrid scheme [29] that combines (post-Newtonian) PN approximations and fits to Teukolsky results [30]; (ii) Fisher parameter estimation techniques to make predictions on the capability of a space-based detector to measure the EMRI parameters, in particular a CS parameter that controls the deviations from GR. We have built *kludge* waveforms in the spirit of [31] and have used them to estimate expected measurement errors for the main parameters describing an EMRI system in DCSMG. We find that for LISA these error estimations have the following order of magnitude: central black hole mass, $\Delta \log M_\bullet \sim 5 \cdot 10^{-3}$; central black hole spin, $\Delta a \sim 5 \cdot 10^{-6} M_\bullet$; orbital eccentricity, $\Delta e_0 \sim 3 \cdot 10^{-7}$; luminosity distance of source, $\Delta \log(D_L/\mu) \sim 2 \cdot 10^{-2}$; and for the CS parameter, ξ , in the combination $\zeta = a\xi$, we find $\Delta \log \zeta \sim 4 \cdot 10^{-2}$. Moreover, we also use this framework to put bounds on the CS parameter, ξ , directly. Assuming that GR is the correct theory to describe EMRIs, we find that LISA measurements could put bounds of the order $\xi^{1/4} < 10^4$ km, which are better by four orders of magnitude than those derived from frame dragging observations around the Earth [32].

This paper is organized as follows. In Section II we describe all the components used for the construction of EMRI gravitational waveforms in DCSMG and the response of space-based GW detectors. This includes the basic aspects of the theory, the deviations in the MBH geometry and its impact in the orbital dynamics and the inclusion of RR effects. In Section III we summarize the basics elements of signal analysis theory and parameter estimation based on Fisher matrix techniques. In Section IV we apply these techniques to the waveforms and response models built in Sec. II, providing parameter error estimates for both LISA and eLISA/NGO and also bounds to the CS parameter. We finish in Section VI with conclusions and a discussion. Appendix A contains the form of the power spectral density of LISA and eLISA/NGO, while Appendix B contains the formulae needed for the construction of the RR effects.

Throughout this paper we use Einstein summation convention for repeated indices and geometrized units in which $G = c = 1$. Spacetime indices are denoted by Greek letters; spatial indices are denoted with Latin letters i, j, \dots ; ∇_μ denotes the canonical metric covariant derivative operator and $\square \equiv g^{\mu\nu} \nabla_\mu \nabla_\nu$ denotes the d’Alambertian wave operator.

II. EMRIS IN DCSMG

In order to carry out parameter estimation studies to assess the ability of a given GW detector to detect and extract the physical information of an EMRI system, we first need a theoretical model of the generated waveforms. EMRIs are complex systems and we do not have yet a description accurate enough to produce waveforms in GR

that can be used for data analysis purposes. However, for parameter estimation studies it is enough to have a waveform model that contains all the features of the real waveforms and that approximates the waveform phase to within a few cycles over the whole inspiral.

Due to the large difference between the masses of the two components in an EMRI, the GW signal can be modeled accurately using perturbation theory (see e.g. [33]), where the SCO is represented as a structureless particle orbiting in the MBH spacetime background. Although on short timescales the orbit of the SCO is approximately a geodesic of the MBH spacetime, its parameters slowly change with time due to RR effects. The best method we have to estimate these RR effects is the so-called *self-force* approach. At present, the gravitational self-force has been computed for the case of a non-rotating MBH [34, 35] and progress is being made towards calculations for the more astrophysically relevant case of a spinning MBH [36] (see [37–39] for reviews).

In parallel to the self-force program, some efforts to build certain approximation schemes to model EMRIs have been made. For the purposes of this work we focus on the so-called *Numerical Kludge* waveform model [31]. In that framework, the orbital motion is given by a sequence of geodesics around a Kerr MBH, with the evolution of the geodesic parameters dictated by a dissipative RR prescription. This prescription is based on PN evolution equations for the orbital elements (from 2PN expressions for the fluxes of energy and angular momentum) calibrated to more accurate Teukolsky fluxes with 45 fitting parameters [29]. The waveforms are then modeled using a multipolar expansion [40].

To accurately compute the GW emission from EMRIs in an alternative theory of gravity, we need to understand both how the orbital dynamics of the binary are altered and how gravitational wave generation and propagation differs in the alternative theory. In DCSMG, the GW emission formulae are not modified at leading order [27], and so in this paper we will consider modifications to the underlying orbital dynamics only. In what follows we describe the main components of our waveform model, summarizing the procedure introduced in [27] and including the RR effects just described.

A. Formulation of DCSMG

In DCSMG the action functional depends on the spacetime metric $g_{\mu\nu}$, on the CS scalar field ϑ , and on the matter fields ψ_{mat} , and it can be cast in the following form

$$S[g_{\mu\nu}, \vartheta, \psi_{\text{mat}}] = \kappa_N S_{\text{EH}}[g_{\mu\nu}] + \frac{\alpha}{4} S_{\text{CS}}[g_{\mu\nu}, \vartheta] + \frac{\beta}{2} S_\vartheta[g_{\mu\nu}, \vartheta] + S_{\text{mat}}[g_{\mu\nu}, \psi_{\text{mat}}], \quad (1)$$

where κ_N is the gravitational constant, $1/(16\pi)$ in geometrized units, and α and β are universal coupling constants that control the strength of the CS modifications.

The different contributions to the action are: the GR Einstein-Hilbert action

$$S_{\text{EH}} = \int d^4x \sqrt{-g} R, \quad (2)$$

where g is the metric determinant and R is the Ricci curvature scalar; the CS gravitational correction

$$S_{\text{CS}} = \int d^4x \sqrt{-g} \vartheta * RR, \quad (3)$$

where $*RR := *R^\alpha{}_\beta{}^{\gamma\delta} R^\beta{}_{\alpha\gamma\delta} = \frac{1}{2} \epsilon^{\gamma\delta\mu\nu} R^\alpha{}_{\beta\mu\nu} R^\beta{}_{\alpha\gamma\delta}$ is the Pontryagin density, $R^\mu{}_{\nu\alpha\beta}$ is the Riemann tensor, $\epsilon^{\mu\nu\alpha\beta}$ is the Levi-Civita antisymmetric tensor and here the asterisk denotes the dual operation; the CS scalar field action term

$$S_\vartheta = - \int d^4x \sqrt{-g} [g^{\mu\nu} (\nabla_\mu \vartheta) (\nabla_\nu \vartheta) + 2V(\vartheta)] , \quad (4)$$

where V is the scalar field potential, which is neglected in this work (i.e. $V = 0$); and finally, $S_{\text{mat}}[g_{\mu\nu}, \psi_{\text{mat}}]$ is the action of the different matter fields.

Varying the action with respect to the metric and the CS scalar field, we obtain the field equations of DCSMG:

$$G_{\mu\nu} + \frac{\alpha}{\kappa_N} C_{\mu\nu} = \frac{1}{2\kappa_N} (T_{\mu\nu}^{\text{mat}} + T_{\mu\nu}^{(\vartheta)}) , \quad (5)$$

$$\beta \square \vartheta = -\frac{\alpha}{4} *RR, \quad (6)$$

where $G_{\mu\nu}$ is the Einstein tensor and $C^{\mu\nu}$ is the so-called C -tensor which has two parts, $C^{\mu\nu} = C_1^{\mu\nu} + C_2^{\mu\nu}$ with

$$C_1^{\alpha\beta} = (\nabla_\sigma \vartheta) \epsilon^{\sigma\delta\nu(\alpha} \nabla_\nu R^{\beta)}{}_\delta ,$$

$$C_2^{\alpha\beta} = (\nabla_\sigma \nabla_\delta \vartheta) *R^{\delta(\alpha\beta)\sigma} . \quad (7)$$

Finally, $T_{\mu\nu}^{\text{mat}}$ is the matter stress-energy tensor and $T_{\mu\nu}^{(\vartheta)}$ is the stress-energy of the CS scalar field, given by

$$T_{\mu\nu}^{(\vartheta)} = \beta \left[(\nabla_\mu \vartheta) (\nabla_\nu \vartheta) - \frac{1}{2} g_{\mu\nu} (\nabla^\sigma \vartheta) (\nabla_\sigma \vartheta) \right] . \quad (8)$$

One can see that taking the divergence of the field equations (5), using the Bianchi identities and the conservation of the matter stress-energy tensor, one obtains the field equation (6) for the CS scalar field.

There are several consequences of DCSMG that are relevant for this work. The first one is that the number of independent waveform polarizations that a detector far away from a GW source will see are the same in DCSMG as in GR [27], i.e., the plus and cross tensor GW polarizations. In addition to the plus and cross polarizations, in DCSMG there is an additional breathing mode, however it decays faster, typically like r^{-2} and is therefore unlikely to be detected by an observer far away from the source. Another important property of GWs in DCSMG is the structure of the stress-energy (or mass) tensor that can be associated with the GWs in the *short-wave* approximation (see, e.g. [41]), commonly known as the Isaacson tensor [42, 43]. In [27] it was shown that the GW

stress-energy tensor has the same form (in terms of the gauge-invariant metric perturbation describing the GWs) as the one of Isaacson for GR. This is due to the fact that the averaging involved in the short-wave approximation cancels out all the CS corrections giving rise, at leading order, to essentially the same backreaction in DCSMG as in GR.

B. The MBH geometry in DCSMG

The first ingredient we need to model the dynamics of an EMRI system is the geometry of the MBH. In GR we know that, provided the *no-hair* conjecture is true, all MBHs must be described by the Kerr metric. However, this is no longer true in DCSMG. We do not have an exact solution in DCSMG for spinning MBHs, but there is an approximate solution [25, 44] that has been found using a small-coupling approximation (using $\zeta_{\text{CS}} \equiv \alpha^2 / (M_\bullet \beta \kappa_N)$ as the expansion parameter, with M_\bullet being the MBH mass) and a slow-rotation approximation (defined by $a/M_\bullet \ll 1$, with $a \equiv |\mathbf{S}_\bullet|/M_\bullet$, $0 \leq a/M_\bullet \leq 1$, and \mathbf{S}_\bullet is MBH spin). Using a system of coordinates that in the GR limit coincide with the well-known Boyer-Lindquist (BL) coordinates (t, r, θ, ϕ) [25], the non-vanishing metric components have the following form

$$g_{tt} = - \left(1 - \frac{2M_\bullet r}{\rho^2} \right) , \quad (9)$$

$$g_{rr} = \frac{\rho^2}{\Delta} , \quad (10)$$

$$g_{\theta\theta} = \rho^2 , \quad (11)$$

$$g_{\phi\phi} = \frac{\Sigma}{\rho^2} \sin^2 \theta , \quad (12)$$

$$g_{t\phi} = \left[\frac{5}{8} \frac{\xi}{M_\bullet^4} \frac{a}{M_\bullet} \frac{M_\bullet^5}{r^4} \left(1 + \frac{12M_\bullet}{7r} + \frac{27M_\bullet^2}{10r^2} \right) - \frac{2M_\bullet a r}{\rho^2} \right] \sin^2 \theta , \quad (13)$$

where we have introduced the following definitions: $\rho^2 = r^2 + a^2 \cos^2 \theta$, $\Delta = r^2 f + a^2$, $f = 1 - 2M_\bullet/r$, and $\Sigma = (r^2 + a^2)^2 - a^2 \Delta \sin^2 \theta$. The effects of the CS gravitational modification are parametrized by a single universal constant, ξ , given by

$$\xi := \frac{\alpha^2}{\beta \kappa_N} . \quad (14)$$

Notice that the only metric component that gets modified with respect to the general relativistic case is the component $g_{t\phi}$ [Eq (13)]. The term in this component that is proportional to the CS parameter ξ falls off with distance as r^{-4} , that is, it decays much faster than the rest of the metric components and hence it becomes negligible at large distances. Only gravitational systems like EMRIs can probe this modification as they penetrate into the strong field region of the MBH.

At the level of approximation at which the DCSMG metric [Eq (13)] was obtained, it is possible to show that it has most of the properties of the Kerr metric [27], in particular the DCSMG metric is stationary and axisymmetric, and also has a Killing tensor, which is important for an analysis of the orbital motion. Moreover, the DCSMG metric has the same algebraic structure as the Kerr one. Regarding the multipolar structure of this DCSMG metric, let us remember that the multipole moments of the Kerr metric are fully determined by the MBH mass and spin (or equivalently, by the mass monopole and current dipole) according to the following simple relations: $M_\ell + iS_\ell = M (ia)^\ell$, where $\{M_\ell\}_{\ell=0,\dots,\infty}$ and $\{S_\ell\}_{\ell=0,\dots,\infty}$ are the mass and current multipole moments respectively. The multipole moments associated with the CS metric deviate from those of Kerr starting at the S_4 multipole, as one can see by employing the multipolar formalism of [40] (see also [45]). Despite this deviation, the structure of these multipole moments still preserves the philosophy of the no-hair conjecture since they only depend on the mass and spin of the MBH. There is also a dependence on the CS parameter ξ , but this is a universal dependence that would be the same for all MBHs and hence it cannot be considered to be *hair* of the MBH.

The equations for the metric and CS scalar field are coupled, so they have to be solved simultaneously. The solution for the CS scalar, at the same level of approximation as for the metric, is:

$$\vartheta = \frac{5}{8} \frac{\alpha}{\beta} \frac{a}{M_\bullet} \frac{\cos \theta}{r^2} \left(1 + \frac{2M_\bullet}{r} + \frac{18M_\bullet^2}{5r^2} \right). \quad (15)$$

This scalar field falls off as r^{-2} and therefore it has a finite energy associated with it.

C. Orbital Kinematics

It was argued in [27] that in DCSMG massive particles should follow geodesics of the spacetime metric. At the lowest order of approximation, and for short periods of time, the trajectory of the SCO can then be approximated by geodesics of the metric given in Eqs. (9)-(13). Actually, we are going to approximate the orbital motion as a sequence of geodesics, as in the GR case within the Numerical Kludge (NK) waveform model. For this reason, it is important to analyze in detail the structure of the geodesic motion around this modified-Kerr metric.

In the previous subsection we mentioned that the modified MBH geometry has essentially the same physical and geometrical properties as the Kerr metric. In particular it has the same number of symmetries. Therefore, we can separate the geodesic equations as in the Kerr case, introducing certain constants of the motion. More specifically, we have the energy per unit SCO mass, E , the angular momentum component along the spin axis per unit SCO mass, L_z , and finally the Carter constant per unit SCO mass squared, C .

The geodesic equations have the following structure [27]:

$$\dot{t} = \dot{t}_K + L_z \delta g_\phi^{\text{CS}}(r), \quad (16)$$

$$\dot{\phi} = \dot{\phi}_K - E \delta g_\phi^{\text{CS}}(r), \quad (17)$$

$$\dot{r}^2 = \dot{r}_K^2 + 2EL_z f \delta g_\phi^{\text{CS}}(r), \quad (18)$$

$$\dot{\theta}^2 = \dot{\theta}_K^2, \quad (19)$$

where the dots denote differentiation with respect to proper time. The quantities $(\dot{t}_K, \dot{r}_K, \dot{\theta}_K, \dot{\phi}_K)$ are the counterparts of the geodesic equations in the Kerr metric, which are given by (see, e.g. [46])

$$\begin{aligned} \rho^2 \dot{t}_K &= -a (a E \sin^2 \theta - L_z) \\ &+ \frac{r^2 + a^2}{\Delta} [(r^2 + a^2) E - a L_z], \end{aligned} \quad (20)$$

$$\rho^2 \dot{\phi}_K = \frac{a}{\Delta} [(r^2 + a^2) E - a L_z] - \left(a E - \frac{L_z}{\sin^2 \theta} \right) \quad (21)$$

$$\begin{aligned} \rho^4 \dot{r}_K^2 &= [(r^2 + a^2) E - a L_z]^2 \\ &- \Delta [Q + (a E - L_z)^2 + r^2], \end{aligned} \quad (22)$$

$$\rho^4 \dot{\theta}_K^2 = Q - \cot^2 \theta L_z^2 - a^2 \cos^2 \theta (1 - E^2), \quad (23)$$

where Q is an alternative definition of the Carter constant, related to C by

$$Q = C - (L_z - a E)^2. \quad (24)$$

It is clear from Eqs. (16)-(18) that the CS deviations are determined by a single function of the radial coordinate r , $\delta g_\phi^{\text{CS}}(r)$, which has the form

$$\delta g_\phi^{\text{CS}} = \frac{\xi a}{112 r^6 f} \left(70 + 120 \frac{M_\bullet}{r} + 189 \frac{M_\bullet^2}{r^2} \right). \quad (25)$$

Only the equation for the polar coordinate θ is unchanged. Since we are dealing with bound orbits, both the radial and the polar motion include turning points (extrema of motion) at which the time derivatives, \dot{r} or $\dot{\theta}$, vanish. This can create numerical problems when integrating the set of Ordinary Differential Equations (ODEs) given by Eqs. (16)-(18). To avoid this, we follow the same strategy as in the case of Kerr geodesics and introduce two angle coordinates, ψ and χ , associated with the radial and polar motion respectively:

$$r = \frac{p M_\bullet}{1 + e \cos \psi}, \quad \cos^2 \theta = \cos^2 \theta_{\min} \cos^2 \chi, \quad (26)$$

where p and e are the dimensionless semilatus rectum and the eccentricity of the orbit respectively, and θ_{\min} is the minimum of θ in the orbit (the turning point in the polar motion). The orbital parameters (e, p) are related with the radial turning points, the apocenter (r_{apo}) and pericenter (r_{peri}), through the standard expressions:

$$r_{\text{peri}} = \frac{p M_\bullet}{1 + e}, \quad r_{\text{apo}} = \frac{p M_\bullet}{1 - e}. \quad (27)$$

or equivalently

$$p = \frac{2r_{\text{peri}}r_{\text{apo}}}{M_{\bullet}(r_{\text{peri}} + r_{\text{apo}})}, \quad e = \frac{r_{\text{apo}} - r_{\text{peri}}}{r_{\text{peri}} + r_{\text{apo}}}. \quad (28)$$

The radial coordinate r oscillates in the interval $(r_{\text{peri}}, r_{\text{apo}})$. Similarly, given the turning point of the polar motion, $\theta_{\text{min}} \in [0, \pi/2]$, θ performs a libration motion in the interval $(\theta_{\text{min}}, \pi - \theta_{\text{min}})$. We introduce the orbital inclination angle (with respect to the spin direction), through the following relation

$$\theta_{\text{inc}} = \text{sign}(L_z) \left[\frac{\pi}{2} - \theta_{\text{min}} \right], \quad (29)$$

where $\text{sign}(L_z) = 1$ corresponds to a prograde orbit and $\text{sign}(L_z) = -1$ corresponds to a retrograde orbit. A different definition of the orbital inclination angle can be given in terms of the constants of motion $(E, L_z, C \text{ or } Q)$

$$\cos \iota = \frac{L_z}{\sqrt{L_z^2 + Q}}. \quad (30)$$

In general, both inclination angles, θ_{inc} and ι , are quite similar [47] and coincide in the non-spinning limit, $a = 0$.

We work with two geodesic parameterizations, one based on the orbital parameters $(e, p, \theta_{\text{inc}} \text{ or } \iota)$ and one based on the *constants* of motion $(E, L_z, C \text{ or } Q)$. Changing from one parameterization to the other is a fundamental step in our computations. In the GR case there is a well-known procedure (see, e.g. [47, 48]) to do so. Here, we have used the implementation described in the appendices of [49]. However, these formulae are only valid in GR and, in our case, the CS modification of the radial equation of motion changes the location of the turning points. In practice this translates into a different relation between the two sets of parameters $(e, p, \theta_{\text{inc}} \text{ or } \iota)$ and $(E, L_z, C \text{ or } Q)$. Given that we are not dealing with large deviations from the GR case, we have used a numerical procedure based on the Newton-Raphson method for finding roots (see, e.g. [50]), where the values obtained from the GR method have been used as the starting point for the iteration algorithm. We have seen that in practice this works quite well and the iteration converges rapidly to the correct values.

Finally, due to the separability of the geodesic equations, which is closely related to the spacetime symmetries, we can distinguish in the motion three *fundamental* frequencies (here with respect to coordinate time t) associated with the radial motion, $f_r = 1/T_r$ (T_r is the average time to go from pericenter to apocenter and back to pericenter), with the polar motion, $f_\theta = 1/T_\theta$ (T_θ is the average time for a full oscillation of the orbital plane, going from $\theta = \theta_{\text{min}}$ to $\theta = \pi - \theta_{\text{min}}$ and back to $\theta = \theta_{\text{min}}$), and $f_\phi = 1/T_\phi$ (T_ϕ is the average time for the SCO's azimuthal angular coordinate ϕ to cover 2π radians). It is important to mention that these frequencies change when including the CS modifications [27].

D. Orbital Dynamics

So far, the orbital dynamics described have been for geodesic orbits. In order to compute the SCO trajectory, we gradually evolve the parameters of the instantaneous geodesic orbit under RR. The RR effects not only drive the SCO inspiral, but also break the degeneracy between orbits in GR and others in DCSMG¹, since a given initial orbital configuration will evolve differently in these theories. Therefore we need to implement RR effects in the EMRI dynamics in the framework of DCSMG.

As we have mentioned above, in this paper we adapt the NK waveform model to the case of DCSMG [31]. In the NK waveform model, the RR driven evolution uses a “hybrid” scheme described in [29], where formulae for the evolution of the *constants* of motion $(E, L_z, C \text{ or } Q)$ are derived in terms of PN approximations (at 2PN order) combined with fits to results from the Teukolsky formalism (see [30, 51]). In principle one should then derive the analogous formulae for the case of DCSMG, but this involves a number of major developments that are currently out of reach. Instead, we will take into account one of the important results about GWs in DCSMG discussed previously — the realization that the stress-energy momentum tensor for GWs, the Isaacson tensor, has the same form in terms of the GW metric perturbation in both theories, GR and DCSMG. This means that, to leading-order, the properties of the GW emission in GR and DCSMG are the same. Then, we approximate the fluxes of energy and angular momentum in the GWs, and also the evolution of the Carter constant under GW emission, by using the GR expressions. In what follows, we describe the formulae and procedures to update the geodesic orbits in our NK-EMRI model.

The evolution equations for the constants of motion $(E, L_z, C \text{ or } Q)$ have the following structure:

$$\frac{dE}{dt} = \mu f_E(a, p, e, \theta_{\text{inc}}), \quad (31)$$

$$\frac{dL_z}{dt} = \mu f_{L_z}(a, p, e, \theta_{\text{inc}}), \quad (32)$$

$$\frac{dQ}{dt} = \mu f_Q(a, p, e, \theta_{\text{inc}}). \quad (33)$$

The evolution equation for C follows from these equations and Eq. (24). The form of the right-hand sides f_E , f_{L_z} , and f_Q of Eqs. (31)-(33) and full details of their derivation can be found in [29]. In Appendix B we summarize the main expressions needed to build these

¹ Without RR effects the phase evolution of an EMRI waveform, in both theories, will be a multiple Fourier series of the three fundamental frequencies, i.e. it will contain harmonics of the type $\exp\{2\pi i f_{m,n,p} t\}$ with $f_{m,n,p} = m f_r + n f_\theta + p f_\phi$. Then, we would be able to associate physical parameters with a given EMRI in both theories, and hence we would not be able to discriminate between them.

right-hand sides and thus evaluate the evolution of the constants of motion.

In practice, there are two ways in which we can use the evolution equations (31)-(33). The first one consists of computing a phase-space trajectory for the orbital parameters by integrating the set of ODEs for the evolution of the energy, E , angular momentum component along the spin axis, L_z , and Carter constant, Q . Once the phase space trajectory $(E(t), L_z(t), Q(t))$ has been computed, these time-dependent constants are used on the right-hand side of the geodesic equations (20)-(23), to construct the inspiral trajectory of the SCO in the Boyer-Lindquist-like coordinates of the MBH spacetime. The second option, the one that we use in this paper, is to consider the extended system of ODEs consisting of Eqs. (20)-(23) and Eqs. (31)-(33) and integrate them together in time. Although this system of ODEs is coupled, there is a clear hierarchical structure, since the subsystem of Eqs. (31)-(33) can in principle be integrated independently of the subsystem of Eqs. (20)-(23), which can be seen as a subsidiary system.

As mentioned before, Eqs. (31)-(33) are in principle only valid in GR. If the true theory of gravity is DCSMG, these evolution equations will contain corrections. At leading order, GW emission in DCSMG takes the same form as in GR [27], but corrections to the fluxes will still arise from the DCSMG modifications to the orbital motion. These corrections were computed for circular orbits in DCSMG in [52], but enter at a high post-Newtonian order. For this reason, we do not make any modifications to the GR expressions but directly employ the fluxes described in Gair and Glampedakis [29]. Although we therefore use the same RR formulae to evolve the trajectory in DCSMG as in GR, this still leads to a different SCO evolution, since the dependence of the orbital elements ($e, p, \theta_{\text{inc}}$ or ι) on the “constants” of motion (E, L_z, C or Q) is different in the two theories, which leads to correspondingly different gravitational waveforms. That is, the mapping between the orbital elements ($e, p, \theta_{\text{inc}}$ or ι) and the *constants* of motion (E, L_z, C or Q) is different in DCSMG and GR. Therefore, given some initial orbital parameters ($e_0, p_0, \theta_{\text{inc},0}$ or ι_0), after evolving the EMRI system for some time, the final orbital parameters in GR will be in general different from the orbital parameters in DCSMG.

Taking into account the previous considerations, the inspiral is constructed in the following way: For a given set of initial orbital parameters ($e_0, p_0, \theta_{\text{inc},0}$ or ι_0), we find the associated initial constants of the motion ($E_0, L_{z,0}, C_0$ or Q_0), which are different from the ones that we would obtain in GR for the same initial eccentricity, semilatus rectum and inclination angle. Subsequently, we evolve the “constants” of motion, $(\dot{E}|_0, \dot{L}_z|_0, \dot{Q}|_0)$, under RR, using the method described above. Then, from the current values of the constant of motion, ($E_0, L_{z,0}, C_0$ or Q_0), their rates of change due to RR, $(\dot{E}|_0, \dot{L}_z|_0, \dot{Q}|_0)$, and the value of the radial period, T_r (the time to go from the apocenter to the pericenter

and back again to apocenter) [27], we obtain the new constants of motion, $(E_1, L_{z,1}, Q_1)$, using the following equations:

$$E_1 = E_0 + \dot{E}|_0 N_r T_r, \quad (34)$$

$$L_{z,1} = L_{z,0} + \dot{L}_z|_0 N_r T_r, \quad (35)$$

$$Q_1 = Q_0 + \dot{Q}|_0 N_r T_r, \quad (36)$$

and N_r is a pre-specified parameter that represents the number of radial periods elapsed between each update of the constants of the motion. The expression for C_1 follows from these formulae for $(E_1, L_{z,1}, Q_1)$ and Eq. (24). Finally from $(E_1, L_{z,1}, C_1/Q_1)$, we obtain the new values of the orbital parameters ($e_1, p_1, \theta_{\text{inc},1}/\iota_1$). This algorithm is iterated along the whole EMRI evolution to obtain the SCO orbit. In Figure 1 we illustrate a section of a generic orbit for a typical system that we use later in our parameter estimation analysis (see Table II).

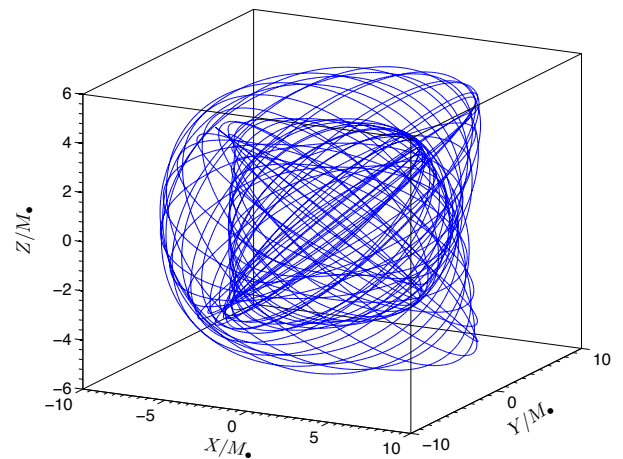


FIG. 1. Depiction of a section of the inspiral orbit for an EMRI (system A in Table II) with parameters $M_\bullet = 5 \cdot 10^5 M_\odot$, $a = 0.25 M_\bullet$, $e_0 = 0.25$ and $\zeta = 5 \cdot 10^{-2} M_\bullet^5$.

E. Waveform Modeling and Detector Responses

In the previous subsections we have seen how the trajectory of the SCO is obtained and, in the following, we describe how we compute the gravitational waveforms and the response of the LISA and eLISA/NGO detectors. Following [31] and [27] we employ the multipolar expansion of the metric perturbations describing the GWs emitted by an isolated system, which assumes that the GWs propagate in a flat background spacetime to reach the observer/detector [40]. In this work, we consider only the lowest-order term, the mass quadrupole. This term involves second time derivatives of the trajectory and these are readily obtained from the geodesic equations (20)-(23). Then, the transverse-traceless (TT)

metric perturbation is computed from the following expression

$$h_{ij}^{\text{TT}}(t) = \frac{2}{r} \ddot{I}_{ij}, \quad (37)$$

where I_{ij} denotes the mass quadrupole and r the luminosity distance from the source to the observer. In terms of the source stress-energy tensor, $T_{\mu\nu}$, the mass quadrupole moment is:

$$I^{ij} = \left[\int d^3x x^i x^j T^{tt}(t, x^i) \right]^{\text{STF}}, \quad (38)$$

where STF stands for symmetric and trace-free. Treating the SCO in the point-mass approximation, the non-vanishing components of the stress energy tensor have the following form: $T^{tt}(t, x^i) = \rho(t, x^i)$ and $T^{tj}(t, x^i) = \rho(t, x^i)v^j(t)$, where $\rho(t, x^i)$ is the energy density of the SCO which, in the point-mass limit, is given by:

$$\rho(t, x^i) = m_* \delta^{(3)}[x^i - z^i(t)], \quad (39)$$

where $\delta^{(3)}$ denotes the three-dimensional Dirac delta distribution, $z^i(t)$ are the spatial Cartesian coordinates (associated with the flat spacetime background) of the SCO trajectory and $v^i(t) = dz^i(t)/dt$ are the components of the corresponding spatial velocity. To evaluate this in our model we make a “particle-on-a-string” approximation, that is we identify the Boyer-Lindquist-like coordinates (r, θ, ϕ) of the SCO’s orbit with flat-space spherical polar coordinates, and introduce Cartesian coordinates in the usual way

$$x = r \sin \theta \cos \phi, \quad y = r \sin \theta \sin \phi, \quad z = r \cos \theta \quad (40)$$

Although this description leads to inconsistencies, like the non-conservation of the flat-space energy-momentum tensor of the particle motion, it has been found to work well when generating EMRI waveforms in GR [31] and so we do not expect this to introduce large errors in the waveforms, in particular in the phase. A possible alternative could be to use coordinate systems more adapted to the multipolar expansion of the gravitational radiation, like harmonic or asymptotic-Cartesian mass-centered coordinates [40] (see also [49]).

We now consider detection of these signals by a space-based detector in a heliocentric orbit (like LISA or eLISA/NGO). We describe the direction from the detector to the EMRI system by a unit 3-vector $\hat{\mathbf{n}}$, which also gives the propagation direction of the GWs from the EMRI to the detector. The orthogonal plane to $\hat{\mathbf{n}}$ is the GW polarization plane and we can introduce there two unit and orthogonal vectors $\hat{\mathbf{p}}$ and $\hat{\mathbf{q}}$ by using the spin direction, $\mathbf{S}_\bullet = aM_\bullet \hat{\mathbf{z}}$:

$$\hat{\mathbf{p}} = \frac{\hat{\mathbf{n}} \times \hat{\mathbf{z}}}{|\hat{\mathbf{n}} \times \hat{\mathbf{z}}|}, \quad \hat{\mathbf{q}} = \hat{\mathbf{p}} \times \hat{\mathbf{n}}. \quad (41)$$

The vectors $(\hat{\mathbf{n}}, \hat{\mathbf{p}}, \hat{\mathbf{q}})$ form a spatial orthonormal basis that can be used to construct the GW polarization tensors:

$$\epsilon_+^{ij} = p_i p_j - q_i q_j, \quad \epsilon_\times^{ij} = 2p_{(i} q_{j)}. \quad (42)$$

The corresponding *plus*, h_+ , and *cross*, h_\times , GW polarizations are given by:

$$h_+(t) = \frac{1}{2} \epsilon_+^{ij} h_{ij}(t), \quad h_\times(t) = \frac{1}{2} \epsilon_\times^{ij} h_{ij}(t), \quad (43)$$

and the complete GW metric perturbation is:

$$h_{ij}(t) = \epsilon_{ij}^+ h_+(t) + \epsilon_{ij}^\times h_\times(t). \quad (44)$$

Using Eqs. (37) and (39) we obtain the following simplified expressions for the GW polarizations in terms of the SCO position $z^i(t)$, velocity $v^i(t) = dz^i/dt$, and acceleration $a^i(t) = d^2 z^i/dt^2$:

$$h_{+, \times}(t) = \frac{2m_*}{r} \epsilon_{ij}^{+, \times} [a^i(t) z^j(t) + v^i(t) v^j(t)]. \quad (45)$$

Once we have the GW waveforms, we compute the response function of a space-based detector in heliocentric motion. Due to the motion of the LISA and eLISA/NGO constellations as they orbit (rotation and translation) it is more convenient to rewrite the response functions in terms of angles defined in a fixed Solar System Barycenter (SSB) coordinate system. The direction from the origin of the SSB reference frame to the origin of the EMRI reference frame is $-\hat{\mathbf{n}}$

$$-\hat{\mathbf{n}} = -(\sin \theta_S \cos \phi_S, \sin \theta_S \sin \phi_S, \cos \theta_S), \quad (46)$$

where (θ_S, ϕ_S) are spherical polar angles that determine the sky location of the EMRI with respect to the SSB frame. The relations between these angles and the angles $(\theta(t), \phi(t))$ that determine the sky location with respect to the detector reference frame are (see, e.g. [53, 54]):

$$\cos \theta(t) = \frac{1}{2} \cos \theta_S - \frac{\sqrt{3}}{2} \sin \theta_S \cos(2\pi t/T - \phi_S), \quad (47)$$

$$\phi(t) = 2\pi t/T + \Phi(t), \quad (48)$$

where

$$\Phi(t) = \tan^{-1} \left[\frac{\sqrt{3} \cos \theta_S + \sin \theta_S \cos(2\pi t/T - \phi_S)}{2 \sin \theta_S \sin(2\pi t/T - \phi_S)} \right] \quad (49)$$

and $T = 1\text{yr}$ is the period of the Earth’s orbit around the Sun. The polarization angle ψ describes the orientation of the “apparent ellipse” given by the projection of the orbit on the sky. It can be written in terms of (θ_S, ϕ_S) and the angles describing the direction of the MBH spin with respect to the SSB reference frame (θ_K, ϕ_K) :

$$\begin{aligned} \tan \psi = & \left[\left\{ \cos \theta_K - \sqrt{3} \sin \theta_K \cos(2\pi t/T - \phi_K) \right\} \right. \\ & - 2 \cos \theta(t) \{ \cos \theta_K \cos \theta_S \\ & + \sin \theta_K \sin \theta_S \cos(\phi_K - \phi_S) \} \left. \right] / \\ & \left[\sin \theta_K \sin \theta_S \sin(\phi_K - \phi_S) \right. \\ & - \sqrt{3} \cos(2\pi t/T) \{ \cos \theta_K \sin \theta_S \sin \phi_S \\ & - \cos \theta_S \sin \theta_K \sin \phi_K \} \\ & - \sqrt{3} \sin(2\pi t/T) \{ \cos \theta_S \sin \theta_K \cos \phi_K \\ & - \cos \theta_K \sin \theta_S \cos \phi_S \} \left. \right]. \quad (50) \end{aligned}$$

In addition, the time of arrival of a gravitational wavefront at the SSB and at the detector will in general differ and are related by

$$t_{\text{SSB}} = t_{\text{D}} + R \sin \theta_{\text{S}} \cos(2\pi t_{\text{D}}/T - \phi_{\text{S}}) - t_{\text{SSB}}^0, \quad (51)$$

where $R = 1$ AU, t_{D} is the time of arrival as seen in the detector reference frame, and t_{SSB}^0 is the initial time in the SSB reference frame:

$$t_{\text{SSB}}^0 = t_{\text{D}}^0 + R \sin \theta_{\text{S}} \cos(2\pi t_{\text{D}}^0/T - \phi_{\text{S}}). \quad (52)$$

This difference in arrival times gives rise to a Doppler modulation in the GW phase measured by LISA. To compute a waveform regularly sampled in time at the detector, we need to generate a waveform unevenly sampled in the source frame (in which the time sampling is the same as at the SSB). This can be achieved employing the relations just introduced.

The response of the detector to an incident GW can then be written as:

$$h_{\alpha}(t) = \frac{\sqrt{3}}{2} [F_{\alpha}^{+}(t)h_{+}(t) + F_{\alpha}^{\times}(t)h_{\times}(t)], \quad (53)$$

where α is an index for the different independent channels of the detector. In the case of LISA we have two independent Michelson-like interferometer channels that can be constructed from the LISA data stream and hence $\alpha = I, II$. By contrast, eLISA/NGO will have only one independent channel (see Appendix A for a brief comparison of the detectors) and hence $\alpha = I$ for eLISA/NGO. The antenna pattern (response) functions, $F_{\alpha}^{+, \times}$, are given by (see, e.g. [54]):

$$F_I^{+} = \frac{1}{2}(1 + \cos^2 \theta) \cos(2\phi) \cos(2\psi) - \cos \theta \sin(2\phi) \sin(2\psi), \quad (54)$$

$$F_I^{\times} = \frac{1}{2}(1 + \cos^2 \theta) \cos(2\phi) \cos(2\psi) + \cos \theta \sin(2\phi) \sin(2\psi), \quad (55)$$

$$F_{II}^{+} = \frac{1}{2}(1 + \cos^2 \theta) \sin(2\phi) \cos(2\psi) + \cos \theta \cos(2\phi) \sin(2\psi), \quad (56)$$

$$F_{II}^{\times} = \frac{1}{2}(1 + \cos^2 \theta) \sin(2\phi) \sin(2\psi) - \cos \theta \cos(2\phi) \cos(2\psi). \quad (57)$$

Here (θ, ϕ, ψ) are as defined in Eqs. (47)–(50) and specify the sky location and orientation of the source in a detector-based coordinate system in terms of angles defined in a fixed SSB coordinate system.

III. ELEMENTS OF SIGNAL ANALYSIS AND MODEL PARAMETER ESTIMATION

The starting point for signal analysis is the detector data stream(s), s_{α} . We assume that s_{α} contains an

EMRI GW signal, h_{α} , and hence we can decompose it as

$$s_{\alpha}(t) = h_{\alpha}(t) + n_{\alpha}(t), \quad (58)$$

where $n_{\alpha}(t)$ is the noise in the detector, which we assume to be stationary, Gaussian and, in the case of LISA, that the two data streams are uncorrelated and the noise power spectral density is the same in each channel. Then, the Fourier components of the noise, which we denote with a tilde $\tilde{n}_{\alpha}(f)$ (see [53, 54] for conventions on the Fourier transform that we use), satisfy

$$\langle \tilde{n}_{\alpha}(f) \tilde{n}_{\beta}^{*}(f') \rangle = \frac{1}{2} \delta_{\alpha\beta} \delta(f - f') S_n(f), \quad (59)$$

where $\langle \cdot \rangle$ denotes expectation value (ensemble average over all possible realizations of the noise), the asterisk now denotes complex conjugation, and $S_n(f)$ is the (one-sided) power spectral density (PSD) of the noise, which is given in Appendix A for both LISA and eLISA/NGO. The assumption of Gaussian noise means that the probability of a particular realization of the noise \mathbf{n}_0 is given by

$$p(\mathbf{n} = \mathbf{n}_0) \propto e^{-(\mathbf{n}_0|\mathbf{n}_0)/2}, \quad (60)$$

where $(\cdot|\cdot)$ denotes the natural inner product in the vector space of signals associated with the PSD $S_n(f)$ and is defined as

$$(\mathbf{a}|\mathbf{b}) = 2 \sum_{\alpha} \int_0^{\infty} df \frac{\tilde{a}_{\alpha}^{*}(f) \tilde{b}_{\alpha}(f) + \tilde{a}_{\alpha}(f) \tilde{b}_{\alpha}^{*}(f)}{S_n(f)}, \quad (61)$$

for any two signals \mathbf{a} and \mathbf{b} . The probability that a given GW signal \mathbf{h} is present in a data stream \mathbf{s} is thus

$$p(\mathbf{s}|\mathbf{h}) \propto e^{-(\mathbf{s}-\mathbf{h}|\mathbf{s}-\mathbf{h})/2}. \quad (62)$$

The ‘best-fit’ waveform will be the one that maximizes $(\mathbf{s}|\mathbf{h})$ and, thus, it provides the maximum likelihood parameter estimate. The expected signal-to-noise ratio (SNR), when filtering with the correct waveform, is

$$\text{SNR} = \frac{(\mathbf{h}|\mathbf{h})}{\text{rms}(\mathbf{h}|\mathbf{n})} = \sqrt{(\mathbf{h}|\mathbf{h})}, \quad (63)$$

where ‘rms’ stands for *root mean square* and the second inequality follows from the fact that the expectation value of $(\mathbf{a}|\mathbf{n})(\mathbf{b}|\mathbf{n})$ is $(\mathbf{a}|\mathbf{b})$ [55]. In practice one considers a waveform template family that will depend on a set of parameters $\boldsymbol{\lambda}$, $\{\mathbf{h}(t, \boldsymbol{\lambda})\}$, and searches for the parameters that maximize the probability of a certain noise realization, i.e., the probability that a given waveform template is present in the data stream. Different realizations of the noise will lead to different values of the best-fit parameters. For large SNR, the best-fit parameters will follow a Gaussian distribution centered around the correct values. Expanding $\exp(-(\mathbf{s}-\mathbf{h}|\mathbf{s}-\mathbf{h})/2)$ around the best-fit parameters, $\boldsymbol{\lambda}_0$, by writing $\boldsymbol{\lambda} = \boldsymbol{\lambda}_0 + \delta\boldsymbol{\lambda}$, we obtain the

following form for the probability distribution function for the errors $\delta\lambda$

$$p(\delta\lambda) = \mathcal{N} \exp\left(-\frac{1}{2}\Gamma_{jk}\delta\lambda^j\delta\lambda^k\right), \quad (64)$$

where $\mathcal{N} = \sqrt{\det(\Gamma/2\pi)}$ is the normalization factor and Γ_{ij} is the *Fisher information matrix* (FM) [56]

$$\Gamma_{jk} = \left(\frac{\partial\mathbf{h}}{\partial\lambda^j} \middle| \frac{\partial\mathbf{h}}{\partial\lambda^k}\right). \quad (65)$$

The variance-covariance matrix for the waveform parameters is given by the inverse of the FM:

$$\langle\delta\lambda^j\delta\lambda^k\rangle = (\Gamma^{-1})^{jk} [1 + O(1/\text{SNR})], \quad (66)$$

and hence, we can estimate the precision with which we will be able to measure a particular parameter, λ^i , by computing the component Γ_{ii}^{-1} of this inverse matrix, that is (see [57] for a detailed discussion):

$$\Delta\lambda^i \equiv \sqrt{\langle(\delta\lambda^i)^2\rangle} \simeq \sqrt{\Gamma_{ii}^{-1}}. \quad (67)$$

A. The Maximum-Mismatch Criterion

Vallisneri [57] provided a consistency criterion to determine whether the SNR is high enough for the FM results to be trustworthy, called the *Maximum-Mismatch Criterion* (MMC). The MMC criterion was suggested to assess when an estimation of the parameter errors based on a FM analysis would be reliable or not. Since the FM, Γ_{ij} , is built from the partial derivatives of the waveform template with respect to the parameters of the model, it can only represent the true GW signal, h_{GW} , correctly if $h(t, \lambda)$ is linear in all the parameters, λ , across a parameter space region of size comparable to the expected parameter errors. This is the regime in which the *Linearized-Signal Approximation* (LSA) is valid. As we increase the SNR the errors become smaller and consequently the LSA is expected to work better. In the regime of validity of the LSA we can expand the waveform template $h(t, \lambda)$ around the *true* source parameters, λ_{tr} , i.e. $\lambda^i = \lambda_{\text{tr}}^i + \delta\lambda^i$ with $\delta\lambda^i$ being a small deviation in the parameters comparable with the parameter estimation error:

$$h(t, \lambda) = h_{\text{tr}} + \delta\lambda^i (\partial_i h)|_{\lambda_{\text{tr}}} + \frac{\delta\lambda^i \delta\lambda^j}{2} (\partial_{ij}^2 h)|_{\lambda_{\text{tr}}} + \dots \quad (68)$$

Then, the likelihood [Eq. (62)] can be approximated as:

$$p(\mathbf{s}|\lambda) \propto \exp\left\{-\frac{(\mathbf{n}|\mathbf{n})}{2} + \delta\lambda^i \delta\lambda^j \frac{(\partial_i \mathbf{h}|\partial_j \mathbf{h})}{2} + \delta\lambda^j (\partial_j \mathbf{h}|\mathbf{n})\right\}, \quad (69)$$

where the waveform template derivatives are evaluated at $\lambda = \lambda_{\text{tr}}$. The applicability of the FM for parameter

estimation is limited by the high-SNR requirement, in the sense that it can be a poor predictor of the amount of information obtained from waveforms depending on several parameters and detected with relatively low SNR. The MMC is given in terms of the ratio, r , of the LSA likelihood [Eq. (69)] to the exact likelihood [Eq. (60)]:

$$2|\log r| = \left(\Delta\lambda^i (\partial_i \mathbf{h})_{\lambda_{\text{tr}}} - \mathbf{Dh} \middle| \Delta\lambda^j (\partial_j \mathbf{h})_{\lambda_{\text{tr}}} - \mathbf{Dh}\right) \quad (70)$$

where $\mathbf{Dh} = \mathbf{h}(\lambda_{\text{tr}}^k + \Delta\lambda^k) - \mathbf{h}(\lambda_{\text{tr}}^k)$ and $\Delta\lambda^i$ is the estimated error from the diagonal components of the inverse of the FM. The MMC is obtained by taking the maximum value of r over all parameters.

The idea behind the MMC is to choose an iso-probability surface as predicted by the FM, and explore it to verify that the difference between the LSA and exact likelihoods is sufficiently small. Ratios, r , below some fiducial value are considered acceptable. If this condition is satisfied, we can believe that the FM is providing a reliable estimate of the parameter estimation errors.

IV. PARAMETER ESTIMATION STUDIES: METHODS AND RESULTS

In this section we describe the different techniques employed in our parameter estimation analysis and present the main results. We begin by characterizing the EMRI parameter space in our studies in DCSMG, $\{\lambda^i\}_{i=1,\dots,N}$. There are 15 parameters (the 14 of GR plus the DCSMG coupling parameter; see Table I for a brief description): $\lambda = \{M_\bullet, a, \mu, e_0, p_0, \theta_{\text{inc},0}, \zeta, \theta_S, \phi_S, \theta_K, \phi_K, D_L, \psi_0, \chi_0, \phi_0\}$, where the subscript 0 refers to the values of the corresponding quantities at the inspiral initial time.

In order to simplify the computations involved in this study, we have restricted ourselves to a five-dimensional subset of the parameter space, given by $\lambda = \{M_\bullet, a, e_0, \zeta, D_L/\mu\}$ (see Table I for their definition). In this subset we have included those parameters that we have found to have the greatest correlation with the parameter $\zeta = a \cdot \xi$ (see Table I), which controls the strength of the CS modifications (notice that in the MBH metric of Eqs. (9)-(13) the CS parameter ξ always appears multiplied by the spin parameter a and this has motivated the introduction of the combined parameter ζ) in a full parameter space investigation. We have also checked that the results we obtain do not change significantly when more parameters are added to the FM study. For the parameter estimation studies we consider two different EMRI systems, *A* and *B*, whose parameters are given in Table II. These two types of systems differ in the values for the MBH mass, $M_\bullet = 5 \cdot 10^5 M_\odot$ for system *A* and $M_\bullet = 10^6 M_\odot$ for system *B*. We fix the luminosity distance to $D_L = 1$ Gpc, which roughly corresponds to the distance where we might expect the closest detectable sources to lie (see, e.g. [58]). Due to the fact that the inspiral time scales as $\sim \mu$ with the mass ratio,

TABLE I. Summary of the parameters that characterize an EMRI system in DCSMG. The angles (θ_S, ϕ_S) and (θ_K, ϕ_K) are spherical polar coordinates with respect to the ecliptic and the subindex 0 stands for values of parameters computed at the initial time. The parameters with physical dimensions are indicated in square brackets. We set the luminosity distance to $D_L = 1$ Gpc.

Parameter	Description
M_\bullet	MBH mass [M_\odot].
$a = \mathbf{S}_\bullet /M_\bullet$	MBH Spin [M_\bullet].
$\mu = m_\star/M_\bullet$	EMRI mass ratio.
e_0	Eccentricity of the particle orbit at t_0 .
p_0	Dimensionless semilatus rectum at t_0 .
$\theta_{\text{inc},0}$	Inclination of the orbit at t_0 .
ζ	$\xi \cdot a$ [M_\bullet^5].
θ_S	EMRI polar angle.
ϕ_S	EMRI azimuthal angle.
θ_K	MBH spin polar angle.
ϕ_K	MBH spin azimuthal angle.
D_L	Distance from the SSB to the EMRI [Gpc].
ψ_0	Angle variable for the radial motion.
χ_0	Angle variable for the polar motion.
ϕ_0	Boyer-Lindquist azimuthal angle.

TABLE II. EMRI systems considered in the parameter estimation analysis. The table shows the values for the parameters that are considered in the FM computation (see Table I for the whole list of parameters). The rest of EMRI parameters employed in our parameter estimation analysis are the same for both systems and their values are: $m_\star = 10 M_\odot$, $\theta_{\text{inc},0} = 0.569$, $\theta_S = \phi_S = 1.57$, $\theta_K = \phi_K = 0.78$, $\psi_0 = \chi_0 = \phi_0 = 0.78$.

System	M_\bullet	a/M_\bullet	e_0	ζ/M_\bullet^5	D_L/μ [Gpc]
A	$5 \cdot 10^5$	0.25	0.25	$5 \cdot 10^{-2}$	$5 \cdot 10^4$
B	10^6	0.25	0.25	$5 \cdot 10^{-2}$	10^5

the system *A* evolves faster than system *B*, which allows us to use smaller evolution times to obtain reliable results in that case.

For these systems we evolve the trajectory using the geodesic equations given in Sec. IIC and the RR equations given in Sec. IID. This is done using the algorithm outlined in Sec. IID. The ODEs that describe geodesic motion are integrated for the angle variables $[\psi(t), \chi(t), \phi(t)]$ using the Bulirsch-Stoer extrapolation method [59] (see [50, 60] for details). The numerical code also contains routines which convert back and forth between the different parameterizations of the orbit in DCSMG; that compute the Cartesian orbital coordinates, velocities, and accelerations, the multiple moments; etc. The equations that evolve the constants of motion, E , L_z and Q are integrated using simple finite difference rules. Then, we use the formulae of Sec. IIE to compute the gravitational waveforms and the detector responses.

In order to study how different the waveforms in DC-

SMG are from GR, we have evolved our EMRI system during 0.5yr employing different values of the CS parameter ξ and the MBH spin a , and we have computed the following overlap function between a DCSMG and a GR waveform template:

$$\mathcal{O}[\mathbf{h}_{\text{GR}}, \mathbf{h}_{\text{CS}}] \equiv \frac{(\mathbf{h}_{\text{GR}}|\mathbf{h}_{\text{CS}})}{\sqrt{(\mathbf{h}_{\text{GR}}|\mathbf{h}_{\text{GR}})(\mathbf{h}_{\text{CS}}|\mathbf{h}_{\text{CS}})}}, \quad (71)$$

which is symmetric, $\mathcal{O}[\mathbf{h}_{\text{GR}}, \mathbf{h}_{\text{CS}}] = \mathcal{O}[\mathbf{h}_{\text{CS}}, \mathbf{h}_{\text{GR}}]$ and has the obvious property: $\mathcal{O}[\mathbf{h}_{\text{GR}}, \mathbf{h}_{\text{GR}}] = \mathcal{O}[\mathbf{h}_{\text{CS}}, \mathbf{h}_{\text{CS}}] = 1$. We also assume that the two waveforms used for this overlap correspond to EMRIs with the same parameters, except for the CS parameter ζ that vanishes for GR waveforms. The standard overlap defined in Eq. (61) has been computed using the FFTW library [61] for the Fourier transforms and simple integration rules. We have computed this normalized overlap for a total of 121 EMRI systems which have 13 fixed parameters: $M_\bullet = 5 \cdot 10^5 M_\odot$, $m_\star = 10 M_\odot$, $e_0 = 0.25$, $p_0 = 11$, $\theta_{\text{inc},0} = 0.569$, $\theta_S = 1.57$, $\phi_S = 1.57$, $\theta_K = 0.329$, $\phi_K = 0.78$, $D_L/\mu = 5 \cdot 10^4$ Gpc, $\psi_0 = 0.78$, $\chi_0 = 0.78$, $\phi_0 = 0.78$, while the spin a/M_\bullet and the CS parameter ξ/M_\bullet^4 are varied in the interval $[0, 0.5]$. The results are shown in Figure 2, where we can see how the projection of \mathbf{h}_{CS} onto \mathbf{h}_{GR} changes by modifying the values of the MBH spin a/M_\bullet and the CS parameter ξ/M_\bullet^4 . In particular, for higher values of a/M_\bullet and ξ/M_\bullet^4 the overlap $\mathcal{O}[\mathbf{h}_{\text{GR}}, \mathbf{h}_{\text{CS}}]$ decreases, since the difference in the evolution of the SCO in GR and CS, produced by the dephasing introduced by the RR, increases [see Eqs. (16)-(18)] and, consequently, the deviations of \mathbf{h}_{CS} from \mathbf{h}_{GR} are enhanced.

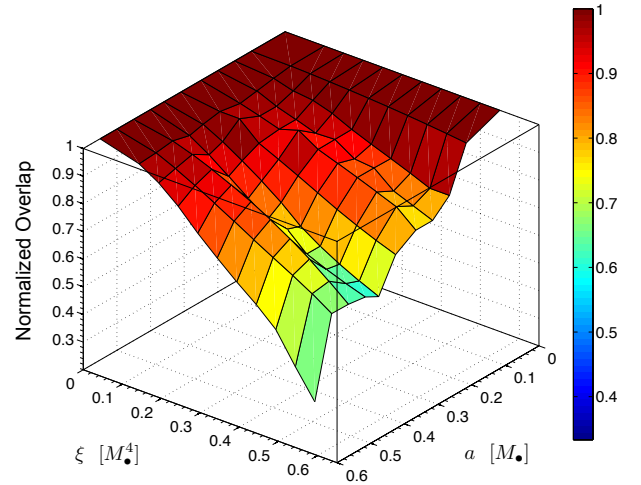


FIG. 2. This 2D plot shows the symmetric normalized overlap of Eq. (71) for EMRI systems with the following parameters: $M_\bullet = 5 \cdot 10^5 M_\odot$, $m_\star = 10 M_\odot$, $e_0 = 0.25$, $p_0 = 11$, $\theta_{\text{inc},0} = 0.569$, $\theta_S = 1.57$, $\phi_S = 1.57$, $\theta_K = 0.329$, $\phi_K = 0.78$, $D_L/\mu = 5 \cdot 10^4$ Gpc, $\psi_0 = 0.78$, $\chi_0 = 0.78$, $\phi_0 = 0.78$. The parameters ξ/M_\bullet^4 and a/M_\bullet take values in the interval $[0, 0.5]$ with a step of 0.05 for a total of 121 points.

We have also obtained the SNR in the frequency domain using Eq. (63). The computation of the FM requires the evaluation of the derivatives of the waveform templates, $\partial_i \mathbf{h} = \partial \mathbf{h} / \partial \lambda^i$ (actually of the response functions of the detector). Since the waveform templates/responses are generated numerically, the corresponding derivatives must also be evaluated numerically. For inner points in the EMRI parameter space (i.e. not near boundaries so that we do not need points outside the proper domains of definition of the parameters) we use the following five-point finite-difference rule:

$$\partial_i \mathbf{h} = \frac{1}{12 \delta \lambda^i} \{ \mathbf{h}(\lambda^i + 2\delta \lambda^i) - \mathbf{h}(\lambda^i - 2\delta \lambda^i) + 8 [\mathbf{h}(\lambda^i + \delta \lambda^i) - \mathbf{h}(\lambda^i - \delta \lambda^i)] \} + O[(\delta \lambda^i)^4] \quad (72)$$

where $\delta \lambda^i$ is the numerical offset in the parameter λ^i . For computations near the boundary or at the boundary of the parameter space we use instead non-centered finite-differences rules. Either the following three-point rule

$$\partial_i \mathbf{h} = \frac{1}{2 \delta \lambda^i} \{ 4\mathbf{h}(\lambda^i + \delta \lambda^i) - \mathbf{h}(\lambda^i + 2\delta \lambda^i) - 3\mathbf{h}(\lambda^i) \} + O[(\delta \lambda^i)^2], \quad (73)$$

or the following four-point rule

$$\partial_i \mathbf{h} = \frac{1}{4 \delta \lambda^i} \{ \mathbf{h}(\lambda^i + 2\delta \lambda^i) - \mathbf{h}(\lambda^i + 3\delta \lambda^i) + 5 [\mathbf{h}(\lambda^i + \delta \lambda^i) - \mathbf{h}(\lambda^i)] \} + O[(\delta \lambda^i)^3]. \quad (74)$$

It is known that computing numerical derivatives is a delicate task (see, e.g. [50]). In the case of finite difference formulas like Eq. (72) the choice of the offset $\delta \lambda^i$ is crucial. An offset too small will produce high-order cancellations in the numerator beyond machine precision. In contrast, an offset too big may mean higher order terms in the Taylor series expansion of the waveform become important. In both cases we will be far from a reasonable approximation. Therefore, we have done investigations that survey wide ranges for $\delta \lambda^i$ in order to find intervals where the derivatives have good convergence properties.

Once we have obtained a FM, Γ_{ij} , that converges in a certain range of offsets $\delta \lambda^i$, we estimate the expected measurement error in the parameters by using Eq. (67). Since FMs for EMRI waveforms have very large condition numbers (the ratio of the largest to the smallest eigenvalues), we use an *LU decomposition* to invert them, writing the matrix as the product of a lower triangular matrix and an upper triangular matrix [62]. In addition, to assess whether the error estimates obtained are reliable or not, we use the MMC defined in Eq. (70). We have evaluated the MMC criterion for all the results presented in this paper and, unless otherwise specified, they satisfy this criterion with values of $|\log r|$ ranging from 10^{-4} to 0.5.

We have stated before that RR effects change the relative phase between waveforms in DCSMG with respect to GR. Now, we are going to study their impact on parameter estimation. Firstly, we will compare the parameter estimation errors for systems evolved under RR and

systems that do not radiate, preserving the constants of motion, i.e. always have the same orbital parameters. These results have been obtained assuming that the detector is LISA. At the end of this section we present some results for eLISA/NGO. The results for system A with and without RR and for different evolution times, $T_{\text{evol}} = 0.1, 0.3, 0.5, 1$ yr, are shown in Table III. The upper part of the table contains the results for the evolutions with RR and the lower part of the table shows the results without RR. In both cases we also show the value of the MMC test, i.e. the quantity $|\log r|$ defined in Eq. (70). We do not show results for $T_{\text{evol}} = 0.1$ yr without RR in Table III since we did not obtain reliable results (according to the MMC criterion). From these results and others we have obtained for other similar EMRI systems we can say that the typical measurement accuracies for the five most important parameters are: $\Delta \log M_\bullet \sim 10^{-3}$, $\Delta a \sim 10^{-6} M_\bullet$, $\Delta e_0 \sim 10^{-7}$, $\Delta \log \zeta \sim 10^{-2}$ and $\Delta \log(D_L/\mu) \sim 10^{-2}$. Comparing the results in Table III, we see that the inclusion of the RR improves the SNR of the signals. It also improves the parameter estimates, in particular those of the spin, a , and of the CS parameter, ζ . This is partially due to the increase of the overall SNR due to RR, but even after rescaling to a fixed reference SNR we see an improvement in the parameter measurement accuracies when RR is included. As one could expect due to the adiabatic nature of the RR (see e.g [63]), the improvement with the inclusion of RR is more significant for longer evolution times.

We can also explore how the error estimates change with the spin parameter a . To that end, we did simulations of systems A and B using the following values of the spin: $a/M_\bullet = 0.1$ (A_1, B_1), $a/M_\bullet = 0.25$ (A_2, B_2), and $a/M_\bullet = 0.5$ (A_3, B_3). The initial semilatus rectum was set to $p_0 = 11 M_\bullet$, which means that after evolving systems A_1 - A_3 for a total time of $T_{\text{evol}} = 0.5$ yr and systems B_1 - B_3 for a total time $T_{\text{evol}} = 1.5$ yr, the final semilatus rectum, p_f , is approximately $8 M_\bullet$ for all systems. The parameter estimation errors are shown in Table IV (the upper part corresponds to simulations of system A whereas the lower part corresponds to simulations of system B). The first thing that we notice is that the smaller the spin parameter a/M_\bullet becomes, the better the parameter estimate for the CS parameter ζ . In particular $\Delta \zeta \sim 2.8 \cdot 10^{-2}$ for system A_1 and $\Delta \zeta \sim 1.4 \cdot 10^{-2}$ for system B_1 . The reason for this is quite simple. The CS modifications affect a single MBH metric component, $g_{t\phi}$ [Eq. (13)], which contains the CS parameter ξ/M_\bullet^4 , multiplied by the spin parameter a . The unperturbed Kerr metric component is proportional to a , and so the relative change in this metric coefficient due to the addition of the DCSMG correction is proportional to ξ . Since we keep $\zeta = a \xi$ fixed as we vary a , the value of ξ increases as a decreases and so the CS correction to the MBH metric is larger relative to the leading order Kerr metric term.

The values of the SNR that we obtain for systems A_1 , A_2 , and A_3 are, 48.1, 46.5, and 44.7 respectively. In the case of systems B_1 , B_2 , and B_3 , the values of the SNR are

TABLE III. Error estimates for LISA and the EMRI system A (see Table II) using RR (upper part of the table) and without using RR (lower part of the table). Each column contains the estimations for a given evolution time ($T_{\text{evol}} = 0.1, 0.3, 0.5, 1$ yr) and shows the corresponding SNR of the EMRI signal.

With RR	$T_{\text{evol}} = 0.1 \text{ yr}$ SNR= 14.5		$T_{\text{evol}} = 0.3 \text{ yr}$ SNR= 43.2		$T_{\text{evol}} = 0.5 \text{ yr}$ SNR= 55.4		$T_{\text{evol}} = 1 \text{ yr}$ SNR= 73.5	
λ^i	$\Delta\lambda^i$	$ \log r $	$\Delta\lambda^i$	$ \log r $	$\Delta\lambda^i$	$ \log r $	$\Delta\lambda^i$	$ \log r $
$\log M_\bullet$	$1.4 \cdot 10^{-1}$	$1.5 \cdot 10^{-1}$	$9.2 \cdot 10^{-3}$	$1.1 \cdot 10^{-1}$	$4.5 \cdot 10^{-3}$	$1.5 \cdot 10^{-1}$	$9.3 \cdot 10^{-4}$	$2.4 \cdot 10^{-1}$
a/M_\bullet	$1.2 \cdot 10^{-4}$	$3.4 \cdot 10^{-1}$	$1.5 \cdot 10^{-5}$	$2.0 \cdot 10^{-1}$	$4.9 \cdot 10^{-6}$	$5.3 \cdot 10^{-2}$	$1.5 \cdot 10^{-6}$	$2.3 \cdot 10^{-1}$
e_0	$5.2 \cdot 10^{-6}$	$5.2 \cdot 10^{-2}$	$9.6 \cdot 10^{-7}$	$3.0 \cdot 10^{-2}$	$5.0 \cdot 10^{-7}$	$9.7 \cdot 10^{-3}$	$2.8 \cdot 10^{-7}$	$6.0 \cdot 10^{-3}$
$\log \zeta$	1.1	$9.3 \cdot 10^{-1}$	$1.5 \cdot 10^{-1}$	$3.1 \cdot 10^{-1}$	$4.9 \cdot 10^{-2}$	$3.1 \cdot 10^{-2}$	$2.0 \cdot 10^{-2}$	$1.5 \cdot 10^{-1}$
$\log(D_L/\mu)$	$2.0 \cdot 10^{-1}$	$2.0 \cdot 10^{-1}$	$1.5 \cdot 10^{-1}$	$4.1 \cdot 10^{-4}$	$1.8 \cdot 10^{-2}$	$1.6 \cdot 10^{-4}$	$1.3 \cdot 10^{-2}$	$2.6 \cdot 10^{-4}$
With no RR	$T_{\text{evol}} = 0.3 \text{ yr}$ SNR= 38.4		$T_{\text{evol}} = 0.5 \text{ yr}$ SNR= 46.8		$T_{\text{evol}} = 1 \text{ yr}$ SNR= 54.6			
λ^i	$\Delta\lambda^i$	$ \log r $	$\Delta\lambda^i$	$ \log r $	$\Delta\lambda^i$	$ \log r $	$\Delta\lambda^i$	$ \log r $
$\log M_\bullet$	$8.3 \cdot 10^{-3}$	$4.3 \cdot 10^{-2}$	$3.9 \cdot 10^{-3}$	$3.7 \cdot 10^{-2}$	$6.6 \cdot 10^{-4}$	$2.3 \cdot 10^{-4}$	$2.3 \cdot 10^{-4}$	$2.3 \cdot 10^{-4}$
a/M_\bullet	$2.3 \cdot 10^{-5}$	$3.3 \cdot 10^{-1}$	$1.4 \cdot 10^{-5}$	$2.4 \cdot 10^{-1}$	$7.4 \cdot 10^{-6}$	$1.6 \cdot 10^{-1}$	$1.6 \cdot 10^{-1}$	$1.6 \cdot 10^{-1}$
e_0	$1.0 \cdot 10^{-6}$	$5.0 \cdot 10^{-2}$	$6.7 \cdot 10^{-7}$	$3.6 \cdot 10^{-2}$	$1.4 \cdot 10^{-6}$	$1.6 \cdot 10^{-3}$	$1.6 \cdot 10^{-3}$	$1.6 \cdot 10^{-3}$
$\log \zeta$	$2.5 \cdot 10^{-1}$	$6.1 \cdot 10^{-1}$	$1.5 \cdot 10^{-1}$	$3.6 \cdot 10^{-1}$	$1.1 \cdot 10^{-1}$	$3.2 \cdot 10^{-1}$	$3.2 \cdot 10^{-1}$	$3.2 \cdot 10^{-1}$
$\log(D_L/\mu)$	$2.8 \cdot 10^{-2}$	$4.8 \cdot 10^{-4}$	$2.1 \cdot 10^{-2}$	$4.8 \cdot 10^{-4}$	$1.8 \cdot 10^{-2}$	$3.8 \cdot 10^{-4}$	$3.8 \cdot 10^{-4}$	$3.8 \cdot 10^{-4}$

50, 46, and 49. Notice that the SNR varies by modifying the value of the spin parameter a , albeit not very much. This dependence of the SNR on the system parameters is expected in the region of the parameter space where the FM can be linearized (see e.g. [64] and [65]).

Overall, the parameter estimation errors for system A have the magnitudes:

$$\Delta \log M_\bullet \sim 5 \cdot 10^{-3}, \quad \Delta a \sim 5 \cdot 10^{-6} M_\bullet, \quad (75)$$

$$\Delta e_0 \sim 3 \cdot 10^{-7}, \quad \Delta \log \zeta \sim 4 \cdot 10^{-2}, \quad (76)$$

$$\Delta \log(D_L/\mu) \sim 2 \cdot 10^{-2}. \quad (77)$$

In the case of system B they are:

$$\Delta \log M_\bullet \sim 6 \cdot 10^{-4}, \quad \Delta a \sim 3 \cdot 10^{-6} M_\bullet, \quad (78)$$

$$\Delta e_0 \sim 10^{-7}, \quad \Delta \log \zeta \sim 2 \cdot 10^{-2}, \quad (79)$$

$$\Delta \log(D_L/\mu) \sim 2 \cdot 10^{-2}. \quad (80)$$

The order of magnitude is roughly the same for both systems, but in general the estimations for system B are better than those for system A , since the MBH mass for system B is larger than the one for system A and the integration time is longer, so there are more observed waveform cycles.

The parameter error estimates presented are for a fixed value of the parameter $\zeta = \xi \cdot a$. Since the spin parameter a/M_\bullet is fixed and is the same for both systems A and B in Table II, this means that in the previous results the CS parameter ξ/M_\bullet^4 was fixed. Now, we present results for the EMRI system A for different values of the CS parameter ξ/M_\bullet^4 . We have considered the following particular values: $\xi = 0.05M_\bullet^4$, $\xi = 0.1M_\bullet^4$ and $\xi = 0.2M_\bullet^4$. The results obtained for the estimation of the parameter errors of $\lambda = \{M_\bullet, a/M_\bullet, e_0, p_0, \zeta, D_L/\mu\}$ are shown in Table V. Due to the fact that the dependence on ξ/M_\bullet^4

and on a/M_\bullet are different in the MBH metric components and in the evolution equations (see Sec. II), one would expect a different dependence of the error estimates when varying both parameters independently. By comparing the results of Tables IV and V, we can see that modifying the value of the CS parameter ξ/M_\bullet^4 only affects significantly the error estimate of the CS parameter itself, whereas modifying a/M_\bullet has a significant effect on the error estimates of all the parameters employed in our study, and in particular on ζ .

Up to now, all the parameter estimation results presented refer to the LISA detector. We now present some results for eLISA/NGO [6]. In order to more easily compare with the results obtained for LISA, we normalize to a fixed SNR, since the SNR for eLISA/NGO is around two times smaller. We considered system A with three different values of the spin parameter a/M_\bullet , namely $a/M_\bullet = 0.1, 0.25$, and 0.5 . The results obtained are quoted in Table VI. Comparing them with the ones quoted in Table IV for LISA, we can see that the parameter estimation accuracy does not change appreciably when the noise curve of LISA is changed for the one of eLISA/NGO and so, all previous results can be considered to apply to eLISA/NGO as well, with the corresponding SNR corrections.

V. PLACING A BOUND ON THE CS PARAMETER

One application of the framework we have developed to perform parameter error studies in DCSMG is to try to put bounds on the CS parameter ξ , which is the combination of CS coupling constants and the gravitational constant that controls deviations from GR in the dynamics of EMRIs. This question has already been investigated in

TABLE IV. Error estimates for LISA and the EMRI systems *A* and *B*. The results shown have been obtained for different values of the initial eccentricity, e_0 , and MBH spin, a . The evolution time for these systems is: $T_{\text{evol}} = 0.5 \text{ yr}$ (system A) and $T_{\text{evol}} = 1.5 \text{ yr}$ (system B). The superscript “†” on a given result indicates that the corresponding Fisher Matrix did not satisfy the MMC criterion, nevertheless we include the results for the sake of completeness.

system A	$e_0 = 0.1$			$e_0 = 0.25$			$e_0 = 0.5$		
a/M_\bullet	0.1	0.25	0.5^\dagger	0.1	0.25	0.5	0.1	0.25	0.5
$\log M_\bullet$	$4.2 \cdot 10^{-3}$	$4.1 \cdot 10^{-3}$	$3.0 \cdot 10^{-3}$	$3.7 \cdot 10^{-3}$	$4.3 \cdot 10^{-3}$	$4.4 \cdot 10^{-3}$	$1.4 \cdot 10^{-3}$	$5.0 \cdot 10^{-3}$	$4.9 \cdot 10^{-3}$
a/M_\bullet	$5.0 \cdot 10^{-5}$	$6.0 \cdot 10^{-6}$	$8.0 \cdot 10^{-6}$	$3.2 \cdot 10^{-6}$	$5.2 \cdot 10^{-6}$	$7.2 \cdot 10^{-6}$	$4.0 \cdot 10^{-6}$	$4.6 \cdot 10^{-6}$	$6.0 \cdot 10^{-6}$
e	$2.3 \cdot 10^{-6}$	$2.4 \cdot 10^{-6}$	$1.4 \cdot 10^{-6}$	$4.9 \cdot 10^{-7}$	$8.6 \cdot 10^{-7}$	$9.2 \cdot 10^{-7}$	$2.0 \cdot 10^{-7}$	$3.3 \cdot 10^{-7}$	$3.3 \cdot 10^{-7}$
$\log \zeta$	$7.5 \cdot 10^{-2}$	$9.9 \cdot 10^{-2}$	$9.0 \cdot 10^{-2}$	$2.8 \cdot 10^{-2}$	$4.9 \cdot 10^{-2}$	$6.6 \cdot 10^{-2}$	$5.1 \cdot 10^{-2}$	$3.5 \cdot 10^{-2}$	$4.3 \cdot 10^{-2}$
$\log(D_L/\mu)$	$1.9 \cdot 10^{-2}$	$2.0 \cdot 10^{-2}$	$2.1 \cdot 10^{-2}$	$1.7 \cdot 10^{-2}$	$2.0 \cdot 10^{-2}$	$2.1 \cdot 10^{-2}$	$1.9 \cdot 10^{-2}$	$2.3 \cdot 10^{-2}$	$2.4 \cdot 10^{-2}$
system B	$e_0 = 0.1$			$e_0 = 0.25$			$e_0 = 0.5$		
a/M_\bullet	0.1	0.25	0.5^\dagger	0.1	0.25	0.5	0.1	0.25	0.5
$\log M_\bullet$	$1.1 \cdot 10^{-3}$	$1.1 \cdot 10^{-3}$	$5.3 \cdot 10^{-4}$	$8.7 \cdot 10^{-4}$	$9.0 \cdot 10^{-4}$	$9.9 \cdot 10^{-4}$	$6.1 \cdot 10^{-4}$	$6.4 \cdot 10^{-4}$	$6.8 \cdot 10^{-4}$
a/M_\bullet	$4.8 \cdot 10^{-6}$	$7.7 \cdot 10^{-6}$	$5.1 \cdot 10^{-6}$	$3.2 \cdot 10^{-6}$	$4.3 \cdot 10^{-6}$	$5.2 \cdot 10^{-6}$	$1.7 \cdot 10^{-6}$	$2.1 \cdot 10^{-6}$	$2.7 \cdot 10^{-6}$
e	$1.5 \cdot 10^{-6}$	$1.9 \cdot 10^{-6}$	$6.0 \cdot 10^{-7}$	$4.1 \cdot 10^{-7}$	$4.3 \cdot 10^{-7}$	$4.5 \cdot 10^{-7}$	$9.6 \cdot 10^{-8}$	$1.0 \cdot 10^{-7}$	$1.1 \cdot 10^{-7}$
$\log \zeta$	$6.4 \cdot 10^{-2}$	$8.5 \cdot 10^{-2}$	$7.0 \cdot 10^{-2}$	$3.7 \cdot 10^{-2}$	$4.3 \cdot 10^{-2}$	$5.3 \cdot 10^{-2}$	$1.3 \cdot 10^{-2}$	$1.6 \cdot 10^{-2}$	$2.1 \cdot 10^{-2}$
$\log(D_L/\mu)$	$2.6 \cdot 10^{-2}$	$2.7 \cdot 10^{-2}$	$2.0 \cdot 10^{-2}$	$2.3 \cdot 10^{-2}$	$2.4 \cdot 10^{-2}$	$2.6 \cdot 10^{-2}$	$2.0 \cdot 10^{-2}$	$2.1 \cdot 10^{-2}$	$2.2 \cdot 10^{-2}$

TABLE V. Error estimates for LISA and the EMRI system *A* in Table II obtained by changing the value of the CS parameter ξ . As we can see, by increasing the value of the CS parameter, ξ , its error estimate, $\Delta \log \zeta$, improves, whereas the rest of the error estimates remain roughly constant.

	$\xi/M_\bullet^4 = 0.05$	$\xi/M_\bullet^4 = 0.1$	$\xi/M_\bullet^4 = 0.2$
$\log M_\bullet$	$4.4 \cdot 10^{-3}$	$4.2 \cdot 10^{-3}$	$4.5 \cdot 10^{-3}$
a/M_\bullet	$4.9 \cdot 10^{-6}$	$4.7 \cdot 10^{-6}$	$4.9 \cdot 10^{-6}$
e_0	$4.9 \cdot 10^{-7}$	$4.9 \cdot 10^{-7}$	$5.0 \cdot 10^{-7}$
$\log \zeta$	$1.9 \cdot 10^{-1}$	$9.5 \cdot 10^{-2}$	$4.9 \cdot 10^{-2}$
$\log(D_L/\mu)$	$1.8 \cdot 10^{-2}$	$1.8 \cdot 10^{-2}$	$1.8 \cdot 10^{-2}$

TABLE VI. Parameter estimation results for eLISA/NGO and the EMRI System *A*. evolved for $T_{\text{evol}} = 2 \text{ yr}$. The corresponding SNR is $\simeq 15$. The value of the initial eccentricity is $e_0 = 0.25$.

	$a/M_\bullet = 0.1$	$a/M_\bullet = 0.25$	$a/M_\bullet = 0.5$
$\log M_\bullet$	$9.0 \cdot 10^{-4}$	$9.8 \cdot 10^{-4}$	$1.3 \cdot 10^{-3}$
a/M_\bullet	$3.2 \cdot 10^{-6}$	$2.8 \cdot 10^{-6}$	$3.9 \cdot 10^{-6}$
e_0	$5.1 \cdot 10^{-7}$	$5.2 \cdot 10^{-7}$	$5.7 \cdot 10^{-7}$
$\log \zeta$	$6.0 \cdot 10^{-2}$	$7.3 \cdot 10^{-2}$	$9.6 \cdot 10^{-2}$
$\log(D_L/\mu)$	$6.4 \cdot 10^{-2}$	$7.0 \cdot 10^{-2}$	$7.5 \cdot 10^{-2}$

the literature, but using astrophysical systems different from EMRIs.

In the case of non-dynamical CS gravity, although the scalar field ϑ has no evolution equation, it can be prescribed a certain time evolution that has an associated time-derivative $\dot{\vartheta}$ and timescale, $\tau_{\text{CS}} = 1/\dot{\vartheta}$. Bounds are normally written in terms of constraints on ℓ^2/τ_{CS} , where ℓ^2 is the characteristic length scale and equals the coupling constant α introduced earlier. Strong bounds on this combination were first obtained by Yunes and Spergel [66] but refinements introduced

by Ali-Haimoud [67] set the bound to 0.2 km, which is three orders of magnitude better than the Solar System bound [68], obtained from data from the LAGEOS satellites orbiting the Earth [69].

For dynamical Chern-Simons gravity, which we consider here, the bound is normally expressed as a bound on $\xi^{1/4}$. The first bound was quoted by Yunes and Pretorius [25] and was $\xi^{1/4} < 10^4 \text{ km}$. However, in a recent paper by Ali-Haimoud and Chen [32] they took into account the fact that the CS solution for the spacetime outside a rotating star is not the same as that outside a rotating black hole, and also that the CS correction can only lead to a decrease in frame-dragging effects and thus cannot be constrained by an upper bound on the precession, but only by a positive lower bound that lies below the GR value. The CS-induced precession that gives the bound quoted in Yunes and Pretorius is two orders of magnitude larger than the GR precession, which means that bound can probably not be trusted. Ali-Haimoud and Chen [32] argue that the best constraints at present are therefore those that come from Solar System measurements, based on data from the Gravity Probe B satellite [70] and also from the LAGEOS satellites [69], which are much weaker. The bound that they get is then $\xi^{1/4} < 10^8 \text{ km}$. In this paper we compare our results with this weaker but more robust bound.

The basis for the computation of our bound is the following. We assume that GR is the correct theory to describe EMRI dynamics and hence assume that measurements made by LISA are compatible with $\xi = 0$. Then, by estimating the error on the measurements of ξ , $\Delta \xi$ [obtained using Eq. (67)], we can set a bound of the following type: $\xi < \Delta \xi$. Different EMRI systems will provide different constraints. But since ξ is a universal quantity, in particular the same for all EMRIs, we just need to look for the EMRI system that provides the best constraint. We have performed several compu-

TABLE VII. Parameter estimation errors for EMRI systems in GR (i.e. on the λ -parameter surface determined by $\xi = \zeta = 0$). The parameters common to all these systems are: $M_\bullet = 5 \cdot 10^5 M_\odot$, $\mu = 2 \cdot 10^{-5}$, $\theta_S = \phi_S = 1.57$ rad, $\theta_K = 0.392$ rad, $\phi_K = 0.78$ rad, $D_L/\mu = 5 \cdot 10^4$ Gpc, and $\psi_0 = \chi_0 = \phi_0 = 0.78$ rad. The last two columns contain the error estimate for the CS parameter ξ and the MMC criterium figure of merit associated with the CS parameter ζ .

a/M_\bullet	e_0	p_0	$\theta_{\text{inc},0}$	T_{evol} (yrs)	$\Delta\xi/M_\bullet^4$	$ \log r $
0.5	0.7	10.0	0.15	0.5	$5.76 \cdot 10^{-8}$	0.91
0.45	0.7	10.0	0.15	0.5	$1.86 \cdot 10^{-7}$	0.84
0.5	0.7	10.0	0.15	0.5	$6.23 \cdot 10^{-8}$	0.89
0.5	0.85	11.0	0.15	0.5	$6.20 \cdot 10^{-8}$	0.7
0.5	0.85	11.0	0.15	1.0	$6.10 \cdot 10^{-8}$	0.57

tations with EMRI systems whose common parameters are: $M_\bullet = 5 \cdot 10^5 M_\odot$, $\mu = 2 \cdot 10^{-5}$, $\theta_S = \phi_S = 1.57$ rad, $\theta_K = 0.392$ rad, $\phi_K = 0.78$ rad, $D_L/\mu = 5 \cdot 10^4$ Gpc, and $\psi_0 = \chi_0 = \phi_0 = 0.78$ rad. We show some relevant results in Table VII for EMRIs with spin parameter $a/M_\bullet \approx 0.5$ (the rest of parameters can be found in the caption of the table). Since we are differentiating about zero, the numerical evaluation of the ξ derivatives must be performed using a one-sided derivative. In particular, we have double-checked some of these results using both the 3-point and 4-point rules given by Eqs. (73) and (74) respectively. We note that, even though we are using system *A* ($M_\bullet = 5 \cdot 10^5 M_\odot$) for this study, the values obtained for the MMC with $T_{\text{evol}} = 0.5$ were slightly above the reference threshold of 0.5 that we used elsewhere in our study. This fact could be connected to using the one-sided derivative in our calculations.

From the error estimates for the ξ parameter shown in Table VII, we find

$$\Delta\xi/M_\bullet^4 < 10^{-7}. \quad (81)$$

which, in suitable units, becomes

$$\xi^{1/4} < 1.4 \cdot 10^4 \text{ km}. \quad (82)$$

This result, a prediction for LISA measurements, is almost four orders of magnitude better than the bound $\xi^{1/4} \lesssim 10^8$ km given in [32]. The corresponding estimate for eLISA/NGO can be found by rescaling the ξ constraint by the SNR, but since the bound scales only as the one-fourth power, the bound for eLISA/NGO is essentially the same.

VI. CONCLUSIONS AND DISCUSSION

In this paper we have examined how well a space-based GW detector like LISA or eLISA/NGO can discriminate between an EMRI system in GR and one occurring in a modified gravity theory like DCSMG. To do this, we have extended previous work in [27] by introducing two key components. The first is the inclusion of RR effects driving the inspiral. We have constructed a waveform template model using an adiabatic-radiative approximation

following the NK waveform model [31]. In this approximation, the inspiral trajectory is modeled as a sequence of geodesics whose constants of motion are updated using formulae for the fluxes of energy, z -component of the angular momentum, and Carter constant, that were derived for general relativistic inspirals in [29] using a combination of PN approximations and fits to results from the Teukolsky formalism.

The second key improvement made in this paper is the use of the Fisher matrix formalism to estimate errors in parameter measurements. We have explored a five-dimensional subspace of the fifteen-dimensional parameter space of EMRIs in DCSMG (see Table I). The parameters that span this subspace are $\{M_\bullet, a/M_\bullet, e_0, \zeta, D_L/\mu\}$. We have focused our studies on two types of systems (see Table II), with masses $10M_\odot + 5 \cdot 10^5 M_\odot$ and $10M_\odot + 10^6 M_\odot$. The parameter error estimates are summarized in Eqs. (77) and (80). For both systems, and assuming a LISA detector, we estimated the measurement error on the logarithm of the CS parameter ζ as $\Delta \log \zeta \sim 10^{-2}$. Therefore, a space-based GW detector like LISA should be able to discriminate between GR and DCSMG. In the case that DCSMG is the correct theory describing the strong gravitational regimes involved in EMRI dynamics, such a detector should be able to provide a good estimation of the CS parameter that controls the deviations from GR. We have also explored how these parameter error estimates change with the spin parameter a/M_\bullet (see Table IV). We have found that by decreasing a/M_\bullet the parameter measurement precision of the CS parameter improves, while modifying the value of ξ (see Table V) does not affect significantly the precision of parameter estimates for the range of other system parameters included in our analysis.

For the case of eLISA/NGO we have presented some parameter error estimation results for system *A* in Table II. In order to compare with LISA results we have normalized these results to a fixed SNR (the eLISA/NGO SNR is approximately a factor of two smaller than the LISA one). Results for three values of the spin parameter ($a/M_\bullet = 0.1, 0.25$, and 0.5) are given in Table VI. The conclusion is that the parameter estimation accuracy at fixed SNR does not change significantly relative to the

LISA results. The LISA results can therefore be applied to eLISA/NGO by applying the appropriate SNR correction.

Finally, we have used our parameter estimation framework to put bounds on the CS parameter ξ . By assuming that GR is the correct theory of gravity we have found that LISA could place a bound $\xi^{1/4} < 1.4 \cdot 10^4$ km, which is almost four orders of magnitude better than the bound obtained in [32] using Solar System data.

The results presented in this paper can be extended in a number of ways by adding more elements to the waveform model that we employ. For example it can be done by: (i) Using a higher order approximation for the MBH geometry in DCSMG; (ii) including CS corrections to the RR formulae, in particular to introduce the effects of the CS scalar field in the RR mechanism; (iii) adding more multipole moments to the gravitational wave expansion formulae; etc. In addition, we have focussed our study on a few EMRI systems, so it would be useful to carry out a more exhaustive study of the parameter space, although this would be a costly task in terms of computational resources. Such extensions to the present work would allow us to consider systems that might be of greater interest from the point of view of improving the parameter estimation results. The approximations underlying our model prevent us from considering systems with spins higher than $a/M_\bullet = 0.5$ and strong CS couplings. However, a better search of the parameter space would allow us to identify systems that provide the best parameter estimates and the strongest bounds on the CS parameter ξ .

There are other extensions of this work that are also interesting. In particular, it would be useful to assess the systematic errors that would arise if GR waveform templates were used to detect EMRIs that are actually described by DCSMG. This could be done using the formalism developed by Cutler and Vallisneri [71] to estimate systematic errors that arise from model uncertainties. Finally, we could apply some of the tools and techniques used in the present work to study other modifications of gravity, different from the CS correction and in this way to exploit the potential of the connection between gravitational wave astronomy and high-energy physics [72].

ACKNOWLEDGMENTS

We would like to thank Leor Barack, Edward K. Porter, Michele Vallisneri, Kent Yagi, and Nicolás Yunes for helpful discussions. PCM work has been supported by a predoctoral FPU fellowship of the Spanish Ministry of Science and Innovation (MICINN) and by the Beatriz de Pinós programme of the Catalan Agency for Research Funding (AGAUR). JG's work is supported by the Royal Society. CFS acknowledges support from the Ramón y Cajal Programme of the Ministry of Education and Science of Spain, by a Marie Curie International Reintegration Grant (MIRG-CT-2007-205005/PHY) within the

7th European Community Framework Programme, from contract 2009-SGR-935 of AGAUR, and from contracts FIS2008-06078-C03-03, AYA-2010-15709, and FIS2011-30145-C03-03 of MICCIN. We acknowledge the computational resources provided by the Barcelona Supercomputing Centre (AECT-2011-3-0007) and CESGA (contracts CESGA-ICTS-200 and CESGA-ICTS-221).

Appendix A: LISA and eLISA Power Spectral Densities

In this paper we assume that the GW detector is either LISA [4, 5] or eLISA/NGO [6]. LISA is a space-based GW detector concept that consists of a quasi-equilateral triangular constellation of three identical spacecrafts with an inter-spacecraft distance of $L = 5 \cdot 10^9$ m. Each spacecraft follows a heliocentric orbit that trails behind the Earth at a distance of $5 \cdot 10^{10}$ m (equivalent to 20 degrees) in such a way that the LISA constellation faces the Sun, slanting at 60 degrees to the ecliptic plane. These particular heliocentric orbits were chosen such that the triangular formation is maintained throughout the year, with the triangle appearing to rotate about the center of the formation once per year. Each spacecraft contains two free-falling test masses whose distance is monitored by 6 laser links. In contrast, the eLISA/NGO constellation has an inter-spacecraft distance of $L = 10^9$ m. Moreover, only one of the spacecrafts will contain two free falling masses and service two arms of the constellation, while the other two will have only one proof mass and service one arm. This effectively reduces the detector response from having two independent Michelson channels to just one.

An essential ingredient required in the detector response is a model for the noise affecting the observations. This may be described in terms of the one-sided noise power spectral density, $S_n(f)$. For LISA, this has three contributions: instrumental noise, $S_n^{\text{inst}}(f)$, confusion noise from short-period galactic binaries, $S_n^{\text{gal}}(f)$, and confusion noise from extragalactic binaries, $S_n^{\text{exgal}}(f)$ [54]:

$$S_n = \min \{ S_n^{\text{inst}} + S_n^{\text{exgal}}, S_n^{\text{inst}} + S_n^{\text{gal}} + S_n^{\text{exgal}} \} \quad (\text{A1})$$

where the different noise contributions are given by:

$$S_n^{\text{inst}}(f) = \exp \left(\kappa T_{\text{mission}}^{-1} \frac{dN}{df} \right) (9.18 \times 10^{-52} f^{-4} + 1.59 \times 10^{-41} + 9.18 \times 10^{-38} f^2) \text{ Hz}^{-1}, \quad (\text{A2})$$

$$S_n^{\text{gal}}(f) = 2.1 \times 10^{-45} \left(\frac{f}{1 \text{ Hz}} \right)^{-7/3} \text{ Hz}^{-1}, \quad (\text{A3})$$

$$S_n^{\text{exgal}}(f) = 4.2 \times 10^{-47} \left(\frac{f}{1 \text{ Hz}} \right)^{-7/3} \text{ Hz}^{-1}, \quad (\text{A4})$$

with dN/df the number density of galactic white dwarf binaries per unit frequency, T_{mission} the lifetime of the

LISA mission, and κ the average number of frequency bins that are lost when each galactic binary is fitted out. The particular values that we use correspond to (see, e.g. [54]) $\kappa \approx 4.5$ and:

$$\frac{dN}{df} = 2 \times 10^{-3} \left(\frac{1\text{Hz}}{f} \right)^{11/3}. \quad (\text{A5})$$

The noise curve for eLISA/NGO is given by [6]:

$$S_n(f) = \frac{4S_{\text{acc}} + S_{\text{sn}} + S_{\text{omn}}}{L^2} \left[1 + \left(\frac{fL}{0.205c} \right)^2 \right] \quad (\text{A6})$$

where S_{acc} , S_{sn} and S_{omn} are, respectively, the power spectral density of the residual acceleration of the test masses, of the shot noise and of other measurement

noises. These are given by:

$$S_{\text{acc}}(f) = 1.37 \cdot 10^{-32} \left(1 + \frac{10^{-4}\text{Hz}}{f} \right) \frac{\text{Hz}}{f^4} \text{m}^2\text{Hz}^{-1} \quad (\text{A7})$$

$$S_{\text{sn}}(f) = 5.25 \cdot 10^{-23} \text{m}^2\text{Hz}^{-1}, \quad (\text{A8})$$

$$S_{\text{omn}} = 6.28 \cdot 10^{-23} \text{m}^2\text{Hz}^{-1}. \quad (\text{A9})$$

Appendix B: Evolution of the Constants of Motion

In [29, 31], to compute EMRIs in general relativity, the fluxes on the right-hand sides of Eqs. (31)-(33) were specified by approximate, weak-field, formulae, augmented with corrections to ensure the behavior was not pathological for near-circular or near-polar orbits and augmented by fits to numerical solutions of the Teukolsky equation. These formulae look as follows (note that in this paper we are using a dimensionless semilatus rectum instead of the semilatus rectum of [29], which has units of M_\bullet):

$$\begin{aligned} \frac{dE}{dt} = (1-e^2)^{3/2} & \left[(1-e^2)^{-3/2} (\dot{E})_{2\text{PN}}(p, \iota, e, a) - (\dot{E})_{2\text{PN}}(p, \iota, 0, a) - \frac{N_4(p, \iota)}{N_1(p, \iota)} (\dot{L}_z)_{2\text{PN}}(p, \iota, 0, a) \right. \\ & \left. - \frac{N_5(p, \iota)}{N_1(p, \iota)} (\dot{Q})_{2\text{PN}}(p, \iota, 0, a) \right], \end{aligned} \quad (\text{B1})$$

$$\frac{dL_z}{dt} = (1-e^2)^{3/2} \left[(1-e^2)^{-3/2} (\dot{L}_z)_{2\text{PN}}(p, \iota, e, a) - (\dot{L}_z)_{2\text{PN}}(p, \iota, 0, a) + (\dot{L}_z)_{\text{fit}} \right], \quad (\text{B2})$$

$$\begin{aligned} \frac{dQ}{dt} = (1-e^2)^{3/2} \sqrt{Q(p, \iota, e, a)} & \left[(1-e^2)^{-3/2} \left(\frac{\dot{Q}}{\sqrt{Q}} \right)_{2\text{PN}}(p, \iota, e, a) - \left(\frac{\dot{Q}}{\sqrt{Q}} \right)_{2\text{PN}}(p, \iota, 0, a) \right. \\ & \left. + 2 \tan \iota \left\{ (\dot{L}_z)_{\text{fit}} + \frac{\sqrt{Q(p, \iota, 0, a)}}{\sin^2 \iota} (i)_{\text{fit}} \right\} \right]. \end{aligned} \quad (\text{B3})$$

where the coefficients N_i 's are

$$N_1(p, \iota) = p M_\bullet^4 \left[p E (p^2 + q^2) - 2q \left(\frac{L_z}{M_\bullet} - qE \right) \right] \Big|_{\text{circ}} \quad (\text{B4})$$

$$N_4(p, \iota) = p M_\bullet^3 \left[(2-p) \frac{L_z}{M_\bullet} - 2qE \right] \Big|_{\text{circ}}, \quad (\text{B5})$$

$$N_5(p, \iota) = \frac{M_\bullet^2}{2} [p(2-p) - q^2] \Big|_{\text{circ}}, \quad (\text{B6})$$

where the subscript ‘circ’ indicated that these coefficients are evaluated for a circular orbit defined by the arguments p and ι . In these expressions, q denotes the di-

mensionless spin parameter of the MBH

$$q = \frac{a}{M_\bullet}, \quad 0 \leq q \leq 1. \quad (\text{B7})$$

In Eqs. (B1)-(B3), the fluxes $(\dot{E})_{2\text{PN}}$, $(\dot{L}_z)_{2\text{PN}}$, and $(\dot{Q})_{2\text{PN}}$ are the 2PN approximations to the averaged evolution of the energy, angular momentum in the spin direction, and Carter constant. They are modifications of the original expressions given in [73] but corrected to avoid unphysical features that they exhibit for nearly circular ($e \approx 0$) and for nearly polar ($\iota \approx \pi/2$) inspirals. The corrected 2PN fluxes have the following form

$$\begin{aligned}
(\dot{E})_{\text{2PN}} = & -\frac{32}{5} \frac{m_\star^2}{M_\bullet^2} \frac{(1-e^2)^{3/2}}{p^5} \left[g_1(e) - \frac{q}{p^{3/2}} g_2(e) \cos \iota - \frac{1}{p} g_3(e) + \frac{\pi}{p^{3/2}} g_4(e) - \frac{1}{p^2} g_5(e) + \frac{q^2}{p^2} g_6(e) \right. \\
& \left. - \left(\frac{527}{96} + \frac{6533}{192} e^2 \right) \frac{q^2}{p^2} \sin^2 \iota \right], \tag{B8}
\end{aligned}$$

$$\begin{aligned}
(\dot{L}_z)_{\text{2PN}} = & -\frac{32}{5} \frac{m_\star^2}{M_\bullet^2} \frac{(1-e^2)^{3/2}}{p^{7/2}} \left[g_9(e) \cos \iota + \frac{q}{p^{3/2}} \{g_{10}^a(e) - g_{10}^b(e) \cos^2 \iota\} - \frac{1}{p} g_{11}(e) \cos \iota \right. \\
& \left. + \frac{\pi}{p^{3/2}} g_{12}(e) \cos \iota - \frac{1}{p^2} g_{13}(e) \cos \iota + \frac{q^2}{p^2} \cos \iota \left\{ g_{14}(e) - \left(\frac{45}{8} + \frac{37}{2} e^2 \right) \sin^2 \iota \right\} \right], \tag{B9}
\end{aligned}$$

$$\begin{aligned}
(\dot{Q})_{\text{2PN}} = & -\frac{64}{5} \frac{m_\star^2}{M_\bullet^2} \frac{(1-e^2)^{3/2}}{p^{7/2}} \sqrt{Q} \sin \iota \left[g_9(e) - \frac{q}{p^{3/2}} g_{10}^b(e) \cos \iota - \frac{1}{p} g_{11}(e) + \frac{\pi}{p^{3/2}} g_{12}(e) \right. \\
& \left. - \frac{1}{p^2} g_{13}(e) + \frac{q^2}{p^2} \left(g_{14}(e) - \frac{45}{8} \sin^2 \iota \right) \right], \tag{B10}
\end{aligned}$$

where the various e -dependent coefficients are

$$\begin{aligned}
g_1(e) &= 1 + \frac{73}{24} e^2 + \frac{37}{96} e^4, & g_2(e) &= \frac{73}{12} + \frac{823}{24} e^2 + \frac{949}{32} e^4 + \frac{491}{192} e^6, & g_3(e) &= \frac{1247}{336} + \frac{9181}{672} e^2, \\
g_4(e) &= 4 + \frac{1375}{48} e^2, & g_5(e) &= \frac{44711}{9072} + \frac{172157}{2592} e^2, & g_6(e) &= \frac{33}{16} + \frac{359}{32} e^2, \\
g_7(e) &= \frac{8191}{672} + \frac{44531}{336} e^2, & g_8(e) &= \frac{3749}{336} - \frac{5143}{168} e^2, & g_9(e) &= 1 + \frac{7}{8} e^2, \\
g_{10}^a(e) &= \frac{61}{24} + \frac{63}{8} e^2 + \frac{95}{64} e^4, & g_{10}^b(e) &= \frac{61}{8} + \frac{91}{4} e^2 + \frac{461}{64} e^4, & g_{11}(e) &= \frac{1247}{336} + \frac{425}{336} e^2, \\
g_{12}(e) &= 4 + \frac{97}{8} e^2, & g_{13}(e) &= \frac{44711}{9072} + \frac{302893}{6048} e^2, & g_{14}(e) &= \frac{33}{16} + \frac{95}{16} e^2. \tag{B11}
\end{aligned}$$

The equation for the evolution for the Carter constant has an additional improvement with respect to the one in [73], where a simple but accurate prescription for the Carter constant was given by assuming that the inclination angle evolution due to GW emission is negligible (see [30, 51] for supporting evidence of this). That is,

$i \approx 0$ leads to $\dot{Q} \approx 2(\dot{L}_z/L_z)Q$ via Eq. (30). The improvement introduced in [29] consists of adding the next-order spin-dependent PN correction.

The final ingredient comes by adding fitting functions to the results of Teukolsky-based computations for circular-inclined orbits [30]. The expressions for the Teukolsky fitted fluxes (to data provided by Scott Hughes) are

$$\begin{aligned}
(\dot{L}_z)_{\text{fit}} = & -\frac{32}{5} \frac{m_\star^2}{M_\bullet} p^{-7/2} \left[\cos \iota + \frac{q}{p^{3/2}} \left(\frac{61}{24} - \frac{61}{8} \cos^2 \iota \right) - \frac{1247}{336 p} \cos \iota + \frac{4\pi}{p^{3/2}} \cos \iota - \frac{44711}{9072 p^2} \cos \iota \right. \\
& + \frac{q^2}{p^2} \cos \iota \left(\frac{33}{16} - \frac{45}{8} \sin^2 \iota \right) + \frac{1}{p^{5/2}} \left\{ q \left(d_1^a + \frac{d_1^b}{p^{1/2}} + \frac{d_1^c}{p} \right) + q^3 \left(d_2^a + \frac{d_2^b}{p^{1/2}} + \frac{d_2^c}{p} \right) \right. \\
& + \cos \iota \left(c_1^a + \frac{c_1^b}{p^{1/2}} + \frac{c_1^c}{p} \right) + q^2 \cos \iota \left(c_2^a + \frac{c_2^b}{p^{1/2}} + \frac{c_2^c}{p} \right) + q^4 \cos \iota \left(c_3^a + \frac{c_3^b}{p^{1/2}} + \frac{c_3^c}{p} \right) \\
& + q \cos^2 \iota \left(c_4^a + \frac{c_4^b}{p^{1/2}} + \frac{c_4^c}{p} \right) + q^3 \cos^2 \iota \left(c_5^a + \frac{c_5^b}{p^{1/2}} + \frac{c_5^c}{p} \right) + q^2 \cos^3 \iota \left(c_6^a + \frac{c_6^b}{p^{1/2}} + \frac{c_6^c}{p} \right) \\
& + q^4 \cos^3 \iota \left(c_7^a + \frac{c_7^b}{p^{1/2}} + \frac{c_7^c}{p} \right) + q^3 \cos^4 \iota \left(c_8^a + \frac{c_8^b}{p^{1/2}} + \frac{c_8^c}{p} \right) + q^4 \cos^5 \iota \left(c_9^a + \frac{c_9^b}{p^{1/2}} + \frac{c_9^c}{p} \right) \left. \right\} \\
& + \frac{q}{p^{7/2}} \cos \iota \left\{ f_1^a + \frac{f_1^b}{p^{1/2}} + q \left(f_2^a + \frac{f_2^b}{p^{1/2}} \right) + q^2 \left(f_3^a + \frac{f_3^b}{p^{1/2}} \right) + \cos^2 \iota \left(f_4^a + \frac{f_4^b}{p^{1/2}} \right) \right. \\
& \left. \left. + q \cos^2 \iota \left(f_5^a + \frac{f_5^b}{p^{1/2}} \right) + q^2 \cos^2 \iota \left(f_6^a + \frac{f_6^b}{p^{1/2}} \right) \right\} \right]. \tag{B12}
\end{aligned}$$

Similarly, a good fit to the evolution of ι is given by

$$\begin{aligned}
(i)_{\text{fit}} = & \frac{32}{5} \frac{m_\star^2}{M_\bullet} \frac{q \sin^2 \iota}{\sqrt{Q}} p^{-5} \left[\frac{61}{24} + \frac{1}{p} \left(d_1^a + \frac{d_1^b}{p^{1/2}} + \frac{d_1^c}{p} \right) + \frac{q^2}{p} \left(d_2^a + \frac{d_2^b}{p^{1/2}} + \frac{d_2^c}{p} \right) + \frac{q}{p^{1/2}} \cos \iota \left(c_{10}^a + \frac{c_{10}^b}{p} + \frac{c_{10}^c}{p^{3/2}} \right) \right. \\
& + \frac{q^2}{p} \cos^2 \iota \left(c_{11}^a + \frac{c_{11}^b}{p^{1/2}} + \frac{c_{11}^c}{p} \right) + \frac{q^3}{p^{5/2}} \cos \iota \left\{ f_7^a + \frac{f_7^b}{p^{1/2}} + q \left(f_8^a + \frac{f_8^b}{p^{1/2}} \right) + \cos^2 \iota \left(f_9^a + \frac{f_9^b}{p^{1/2}} \right) \right. \\
& \left. \left. + q \cos^2 \iota \left(f_{10}^a + \frac{f_{10}^b}{p^{1/2}} \right) \right\} \right], \tag{B13}
\end{aligned}$$

where the values of the numerical fitting coefficients are:

$$\begin{aligned}
d_1^a &= -10.7420, & d_1^b &= 28.5942, & d_1^c &= -9.07738, & d_2^a &= -1.42836, & d_2^b &= 10.7003, \\
d_2^c &= -33.7090, & c_1^a &= -28.1517, & c_1^b &= 60.9607, & c_1^c &= 40.9998, & c_2^a &= -0.348161, \\
c_2^b &= 2.37258, & c_2^c &= -66.6584, & c_3^a &= -0.715392, & c_3^b &= 3.21593, & c_3^c &= 5.28888, \\
c_4^a &= -7.61034, & c_4^b &= 128.878, & c_4^c &= -475.465, & c_5^a &= 12.2908, & c_5^b &= -113.125, \\
c_5^c &= 306.119, & c_6^a &= 40.9259, & c_6^b &= -347.271, & c_6^c &= 886.503, & c_7^a &= -25.4831, \\
c_7^b &= 224.227, & c_7^c &= -490.982, & c_8^a &= -9.00634, & c_8^b &= 91.1767, & c_8^c &= -297.002, \\
c_9^a &= -0.645000, & c_9^b &= -5.13592, & c_9^c &= 47.1982, & f_1^a &= -283.955, & f_1^b &= 736.209, \\
f_2^a &= 483.266, & f_2^b &= -1325.19, & f_3^a &= -219.224, & f_3^b &= 634.499, & f_4^a &= -25.8203, \\
f_4^b &= 82.0780, & f_5^a &= 301.478, & f_5^b &= -904.161, & f_6^a &= -271.966, & f_6^b &= 827.319. \tag{B14}
\end{aligned}$$

$$\begin{aligned}
c_{10}^a &= -0.0309341, & c_{10}^b &= -22.2416, & c_{10}^c &= 7.55265, & c_{11}^a &= -3.33476, & c_{11}^b &= 22.7013, \\
c_{11}^c &= -12.4700, & f_7^a &= -162.268, & f_7^b &= 247.168, & f_8^a &= 152.125, & f_8^b &= -182.165, \\
f_9^a &= 184.465, & f_9^b &= -267.553, & f_{10}^a &= -188.132, & f_{10}^b &= 254.067. \tag{B15}
\end{aligned}$$

-
- [1] D. Psaltis and T. Johannsen, J. Phys. Conf. Ser., **283**, 012030 (2011), arXiv:1012.1602 [astro-ph.HE].
- [2] P. Amaro-Seoane, J. R. Gair, M. Freitag, M. C. Miller, I. Mandel, *et al.*, Class. Quant. Grav., **24**, R113 (2007), arXiv:astro-ph/0703495 [ASTRO-PH].
- [3] P. Amaro-Seoane and M. Preto, Class. Quant. Grav., **28**, 094017 (2011), arXiv:1010.5781 [astro-ph.CO].
- [4] K. Danzmann and A. Rudiger, Class. Quant. Grav., **20**, S1 (2003).
- [5] T. Prince, in *Bulletin of the American Astronomical Society*, Vol. 35 (2003) p. 751.
- [6] P. Amaro-Seoane, S. Aoudia, S. Babak, P. Binetruy, E. Berti, *et al.*, (2012), arXiv:1201.3621 [astro-ph.CO].
- [7] P. Amaro-Seoane, S. Aoudia, S. Babak, P. Binetruy, E. Berti, *et al.*, (2012), arXiv:1202.0839 [gr-qc].
- [8] S. Sigurdsson and M. Rees, Mon. Not. Roy. Astron. Soc., **284**, 318 (1996), arXiv:astro-ph/9608093 [astro-ph].
- [9] L. S. Finn and K. S. Thorne, Phys. Rev., **D62**, 124021 (2000), arXiv:gr-qc/0007074 [gr-qc].
- [10] F. D. Ryan, Phys. Rev., **D52**, 5707 (1995).
- [11] C. F. Sopuerta, GW Notes, **4**, 3 (2010), arXiv:1009.1402 [astro-ph.CO].
- [12] N. A. Collins and S. A. Hughes, Phys. Rev., **D69**, 124022 (2004), arXiv:gr-qc/0402063.
- [13] K. Glampedakis and S. Babak, Class. Quant. Grav., **23**, 4167 (2006), arXiv:gr-qc/0510057.
- [14] J. R. Gair, C. Li, and I. Mandel, Phys. Rev., **D77**, 024035 (2008), arXiv:0708.0628 [gr-qc].
- [15] L. Barack and C. Cutler, Phys. Rev., **D75**, 042003 (2007), arXiv:gr-qc/0612029.
- [16] S. J. Vigeland and S. A. Hughes, Phys. Rev., **D81**, 024030 (2010), arXiv:0911.1756 [gr-qc].
- [17] R. P. Kerr, Phys. Rev. Lett., **11**, 237 (1963).
- [18] R. Jackiw and S. Y. Pi, Phys. Rev., **D68**, 104012 (2003), gr-qc/0308071.
- [19] J. Polchinski, *String theory. Vol. 2: Superstring theory and beyond* (Cambridge University Press, Cambridge, UK, 1998).
- [20] V. Taveras and N. Yunes, Phys. Rev., **D78**, 064070 (2008), arXiv:0807.2652 [gr-qc].
- [21] G. Calcagni and S. Mercuri, Phys. Rev., **D79**, 084004 (2009), arXiv:0902.0957 [gr-qc].
- [22] S. Mercuri and V. Taveras, Phys. Rev., **D80**, 104007 (2009), arXiv:0903.4407 [gr-qc].
- [23] S. Weinberg, Phys. Rev., **D77**, 123541 (2008), arXiv:0804.4291 [hep-th].
- [24] N. Yunes and C. F. Sopuerta, Phys. Rev., **D77**, 064007 (2008), arXiv:0712.1028 [gr-qc].
- [25] N. Yunes and F. Pretorius, Phys. Rev., **D79**, 084043 (2009), arXiv:0902.4669 [gr-qc].
- [26] S. Alexander and N. Yunes, Phys. Rept., **480**, 1 (2009), arXiv:0907.2562 [hep-th].
- [27] C. F. Sopuerta and N. Yunes, Phys. Rev., **D80**, 064006 (2009), arXiv:0904.4501 [gr-qc].
- [28] P. Pani, V. Cardoso, and L. Gualtieri, Phys. Rev., **D83**, 104048 (2011), arXiv:1104.1183 [gr-qc].
- [29] J. R. Gair and K. Glampedakis, Phys. Rev., **D73**, 064037 (2006), arXiv:gr-qc/0510129 [gr-qc].
- [30] S. A. Hughes, Phys. Rev., **D61**, 084004 (2000).
- [31] S. Babak, H. Fang, J. R. Gair, K. Glampedakis, and S. A. Hughes, Phys. Rev., **D75**, 024005 (2007), arXiv:gr-qc/0607007 [gr-qc].
- [32] Y. Ali-Haïmoud and Y. Chen, Phys. Rev., **D84**, 124033 (2011), arXiv:1110.5329 [astro-ph.HE].
- [33] S. Drasco and S. A. Hughes, Phys. Rev., **D73**, 024027 (2006), arXiv:gr-qc/0509101 [gr-qc].
- [34] L. Barack and N. Sago, Phys. Rev. Lett., **102**, 191101 (2009), arXiv:0902.0573 [gr-qc].
- [35] L. Barack and N. Sago, Phys. Rev., **D81**, 084021 (2010), arXiv:1002.2386 [gr-qc].
- [36] A. G. Shah, T. S. Keidl, J. L. Friedman, D.-H. Kim, and L. R. Price, Phys. Rev., **D83**, 064018 (2011), arXiv:1009.4876 [gr-qc].
- [37] L. Barack, Class. Quant. Grav., **26**, 213001 (2009), arXiv:0908.1664 [gr-qc].
- [38] E. Poisson, A. Pound, and I. Vega, (2011), arXiv:1102.0529 [gr-qc].
- [39] J. Thornburg, (2011), arXiv:1102.2857 [gr-qc].
- [40] K. S. Thorne, Rev. Mod. Phys., **52**, 299 (1980).
- [41] C. W. Misner, K. Thorne, and J. A. Wheeler, *Gravitation* (W. H. Freeman & Co., San Francisco, 1973).
- [42] R. A. Isaacson, Phys. Rev., **166**, 1263 (1968).
- [43] R. A. Isaacson, Phys. Rev., **166**, 1272 (1968).
- [44] K. Konno, T. Matsuyama, and S. Tanda, Prog. Theor. Phys., **122**, 561 (2009), arXiv:0902.4767 [gr-qc].
- [45] Y. Gürsel, Gen. Rel. Grav., **15**, 737 (1983).
- [46] S. Chandrasekhar, *The mathematical theory of black holes* (Oxford University Press, New York, 1992).
- [47] S. Drasco and S. A. Hughes, Phys. Rev., **D69**, 044015 (2004), arXiv:astro-ph/0308479 [astro-ph].
- [48] W. Schmidt, Class. Quant. Grav., **19**, 2743 (2002), arXiv:gr-qc/0202090.
- [49] C. F. Sopuerta and N. Yunes, Phys. Rev., **D84**, 124060 (2011), arXiv:1109.0572 [gr-qc].
- [50] W. H. Press, B. P. Flannery, S. A. Teukolsky, and W. T. Vetterling, *Numerical Recipes: The Art of Scientific Computing* (Cambridge University Press, Cambridge (UK) and New York, 1992).
- [51] S. A. Hughes, Phys. Rev., **D64**, 064004 (2001).
- [52] J. Gair and N. Yunes, Phys. Rev., **D84**, 064016 (2011), arXiv:1106.6313 [gr-qc].
- [53] C. Cutler, Phys. Rev., **D57**, 7089 (1998).
- [54] L. Barack and C. Cutler, Phys. Rev., **D69**, 082005 (2004), arXiv:gr-qc/0310125 [gr-qc].
- [55] C. Cutler and E. E. Flanagan, Phys. Rev., **D49**, 2658 (1994), arXiv:gr-qc/9402014 [gr-qc].
- [56] R. A. Fisher, Roy. Stat. Soc. J., **98**, 39 (1935).
- [57] M. Vallisneri, Phys. Rev., **D77**, 042001 (2008), arXiv:gr-qc/0703086 [gr-qc].
- [58] S. Sigurdsson, Class. Quant. Grav., **14**, 1425 (1997), arXiv:astro-ph/9701079 [astro-ph].
- [59] R. Bulirsch and J. Stoer, Num. Math., **8**, 1 (1966).
- [60] J. Stoer and R. Bulirsch, *Introduction to Numerical Analysis* (Springer-Verlag, New York, 1993).
- [61] M. Frigo and S. G. Johnson, Proceedings of the IEEE, **93**, 216 (2005), special issue on "Program Generation, Optimization, and Platform Adaptation".
- [62] E. A. Huerta and J. R. Gair, Phys. Rev., **D79**, 084021 (2009), arXiv:0812.4208 [gr-qc].
- [63] N. Sago, T. Tanaka, W. Hikida, and H. Nakano, Prog. Theor. Phys., **114**, 509 (2005), arXiv:gr-qc/0506092 [gr-qc].

- [64] D. Nicholson and A. Vecchio, Phys. Rev., **D57**, 4588 (1998), arXiv:gr-qc/9705064 [gr-qc].
- [65] A. Stroeer and A. Vecchio, Class. Quant. Grav., **23**, S809 (2006), arXiv:astro-ph/0605227 [astro-ph].
- [66] N. Yunes and D. N. Spergel, Phys. Rev., **D80**, 042004 (2009), arXiv:0810.5541 [gr-qc].
- [67] Y. Ali-Haïmoud, Phys. Rev., **D83**, 124050 (2011), arXiv:1105.0009 [astro-ph.HE].
- [68] T. L. Smith, A. L. Erickcek, R. R. Caldwell, and M. Kamionkowski, Phys.Rev., **D77**, 024015 (2008), arXiv:0708.0001 [astro-ph].
- [69] I. Ciufolini and E. Pavlis, Nature, **431**, 958 (2004).
- [70] C. Everitt, D. DeBra, B. Parkinson, J. Turneaure, J. Conklin, *et al.*, Phys. Rev. Lett., **106**, 221101 (2011), arXiv:1105.3456 [gr-qc].
- [71] C. Cutler and M. Vallisneri, Phys. Rev., **D76**, 104018 (2007), arXiv:0707.2982 [gr-qc].
- [72] V. Cardoso, L. Gualtieri, C. Herdeiro, U. Sperhake, P. M. Chesler, *et al.*, (2012), arXiv:1201.5118 [hep-th].
- [73] K. Glampedakis, S. A. Hughes, and D. Kennefick, Phys. Rev., **D66**, 064005 (2002), arXiv:gr-qc/0205033 [gr-qc].